catalysts

MDPI

Review

Co-Doped, Tri-Doped, and Rare-Earth-Doped g-C_3N_4 for Photocatalytic Applications: State-of-the-Art

Bao Lee Phoon [1], Chong Cheen Ong [2,3], Kuan-Ching Lee [4], Guan-Ting Pan [5,*], Bey Fen Leo [1,6,*], Siewhui Chong [7] and Kuan-Lun Pan [8]

[1] Nanotechnology & Catalysis Research Centre (NANOCAT), Institute for Advanced Studies, IPS Building, Universiti Malaya, Kuala Lumpur 50603, Malaysia; phoonpauline@um.edu.my
[2] Department of Fundamental & Applied Sciences, Universiti Teknologi PETRONAS, Seri Iskandar 32610, Perak Darul Ridzuan, Malaysia; chongcheen92@gmail.com
[3] Centre of Innovative Nanostructures & Nanodevices (COINN), Universiti Teknologi PETRONAS, Seri Iskandar 32610, Perak Darul Ridzuan, Malaysia
[4] Department of Chemical and Environmental Engineering, University of Nottingham Malaysia, Jalan Broga 43500, Selangor, Malaysia; zzzdenny777@gmail.com
[5] Department of Chemical Engineering and Biotechnology, National Taipei University of Technology, Taipei 106, Taiwan
[6] Department of Molecular Medicine, Faculty of Medicine, Universiti Malaya, Kuala Lumpur 50603, Malaysia
[7] Department of Chemical Engineering, Lee Kong Chian Faculty of Engineering and Science, Universiti Tunku Abdul Rahman, Bandar Sg. Long, Kajang 43000, Selangor, Malaysia; faye1004@gmail.com
[8] Industrial Technology Research Institute, Green Energy and Environment Institute, No.195, Sec. 4, Zhongxiao Rd., Zhudong Township, Hsinchu 310, Taiwan; klpan@itri.org.tw
* Correspondence: t6679013@gmail.com (G.-T.P.); beyfenleo@um.edu.my (B.F.L.)

Citation: Phoon, B.L.; Ong, C.C.; Lee, K.-C.; Pan, G.-T.; Leo, B.F.; Chong, S.; Pan, K.-L. Co-Doped, Tri-Doped, and Rare-Earth-Doped g-C_3N_4 for Photocatalytic Applications: State-of-the-Art. *Catalysts* **2022**, *12*, 586. https://doi.org/10.3390/catal12060586

Academic Editor: Bishweshwar Pant

Received: 29 April 2022
Accepted: 24 May 2022
Published: 27 May 2022

Abstract: Rapid industrialization and overpopulation have led to energy shortages and environmental pollution, accelerating research to solve the issues. Currently, metal-free photocatalysts have gained the intensive attention of scientists due to their environmental-friendly nature and ease of preparation. It was noticed that g-C_3N_4 (GCN) consists of a few outstanding properties that could be used for various applications such as water treatment and clean energy production. Nonetheless, bare GCN contains several drawbacks such as high charge recombination, limited surface area, and low light sensitivity. Several solutions have been applied to overcome GCN limitations. Co-doping, tri-doping, and rare-earth-doping can be effective solutions to modify the GCN structure and improve its performance toward photocatalysis. This review highlights the function of multi-elemental and rare-earth dopants in GCN structure, mechanisms, and performance for photocatalytic applications as well as the advantages of co-doping, tri-doping, and rare-earth-doping of GCN. This review summarizes the different roles of dopants in addressing the limitations of GCN. Therefore, this article critically reviewed how multi-elemental and rare-earth-doping affect GCN properties and enhanced photoactivity for various applications.

Keywords: Co-doping; tri-doping; rare-earth-doping; g-C_3N_4; metal-based; non-metal-based; photocatalysis

1. Introduction

Environmental issues and increasing energy demand are among the top challenges today. Contaminants appear to be accumulating over time, reaching harmful levels. During the industrial revolution in the late 18th to early 19th century, non-renewable resources such as fossil fuels are commonly used as raw materials for power generation. Nonetheless, the use of fossil fuels such as petroleum and coal have the potential to cause the greenhouse effect due to the emission of CO_2, NO_x, and SO_2, which can further escalate global warming potential. Apart from that, it was reported that up to 4.1 billion metric tons of CO_2 have been released into the environment in the past decade, and it was expected that the CO_2 emission

will be doubled in the following 10 years [1]. The combustion of fossil fuels can also produce particulate matter ($PM_{2.5}$). It was estimated that approximately 10.2 million deaths per year were due to $PM_{2.5}$, which caused lower respiratory infections for children below 5 years old [2]. Therefore, researchers are taking the initiative to look for alternative power generation methods to achieve zero emission. Apart from energy, wastewater pollution is another threat to the world. There are miscellaneous pollutants such as pharmaceutical products [3,4], textile industry dyes [5], endocrine disruptors (ED) [6], heavy metals [7], and pesticides [8] which can potentially bring harm to the public. For example, United Nations (UN) environment specialists were advised that the thoughtless disposal of antibiotic wastes could produce "ferocious superbugs" [9]. In Korea, antibiotics were detected in more than 80% of the wastewater, drinking water, as well as surface water [10]. From a public health perspective, antibiotics could result in allergic reactions if they exist in domestic used water [11]. ED such as phthalate can interfere with the human endocrine system. Exposure to ED in pregnant women can affect infants at the prenatal level and potentially decline male fertility [12]. Meanwhile, dyes and pesticides in the water bodies, air, and soil can cause a threat to human health [13]. Since water is basic to life, water contamination issues have been of great importance. To date, these kinds of emerging waste are unable to be completely treated by conventional wastewater treatment [4].

Several methods can deal with the above issues. One of the inexpensive and efficient methods is photocatalysis. As shown in Figure 1, photocatalysis is a process that only requires sunlight, oxygen, and a photocatalyst to perform it. Most importantly, this process does not generate secondary waste and is able to tackle environmental issues efficiently. When sunlight penetrates, an electron from the valence band (VB) will jump to the conduction band (CB) due to excitation, leaving a hole in VB. Holes at the VB will undergo oxidation, whereas reduction is carried out at CB with electrons, creating radicals for photoreaction. Photocatalysis is not only able to break down organic pollutants, but it can also perform water splitting, CO_2 conversion to fuel, chemical reactions, and nitrogen fixation.

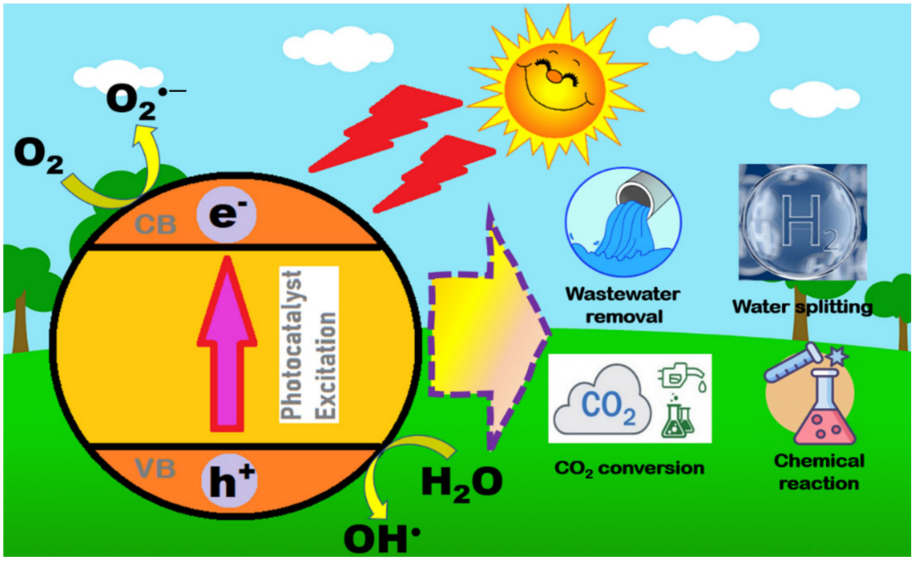

Figure 1. The mechanism of the photocatalytic process and its applications.

Numerous semiconductors with photocatalytic properties are available, for instance, TiO_2 [14], ZnO [15], and $SrTiO_3$ [16,17]. However, these photocatalysts are not visible-light active due to the large bandgap. Graphitic carbon nitride (GCN) is a metal-free n-type photocatalyst. With the low energy bandgap of 2.7 eV, in other words, it can be photoactive under irradiation of solar (λ < 459 nm) [18]. Sometimes, the bandgap of GCN can be varied due to different preparation methods. For example, the bandgap of urea-synthesized GCN was 2.8 eV [19], but melamine-prepared GCN shows 2.6 eV of bandgap energy [20]. Moreover, it was reported that the thermal polymerization temperature can affect the GCN

bandgap as well [21]. In recent years, GCN became of interest to study due to its unique properties. Nevertheless, the pure GCN itself consists of some drawbacks, which are the high recombination rate and insufficient sunlight absorption that limit its performance [22]. Thus, scientists have made numerous efforts to boost the GCN photocatalytic activity by methods such as elemental doping and heterojunction.

Based on Figure 2, the number of reports on GCN materials itself has increased exponentially over the past 15 years. At the same time, nearly 30,000 research works have been reported in the past 10 years for different applications. This demonstrates the attraction and importance of this research area. With the accelerated number of publications in GCN materials, some researchers have published comprehensive reviews in prestigious journals. Patnaik et al. reviewed the performance of anion-doped GCN, but co-doped GCN is not discussed in depth and is only focused on anion [23]. Zhao et al. have researched GCN, but the authors only discussed GCN-based heterojunctions [24]. Liu et al. discussed both metal and non-metal doped GCN, but it is focused on single doping [25]. However, co-doped, tri-doped, and rare-earth-doped GCN and its performance in several applications are not comprehensively discussed. As far as we are concerned, co-doped, tri-doped, and rare-earth-doped GCN has never been critically reviewed by any researchers. In recent years, co-doped, tri-doped, and rare-earth-doped GCN have received great attention for research because they can improve the surface area, reduce the recombination rate, and decrease the bandgap energy. For example, the co-doped GCN reported by Ma et al. was shown to have 27 times greater photoactivity compared to pure GCN and six times greater photoactivity compared to single-doped GCN [26]. Compared to single doping, co-doping has a synergetic effect on the dopants. Thus, this review can facilitate the further developments of new GCN-based materials as well as improve the technology and performance of its applications. Thus, the performance of co-doped, tri-doped, and rare-earth-doped GCN and how they improve the GCN photoactivity will be discussed critically in this review.

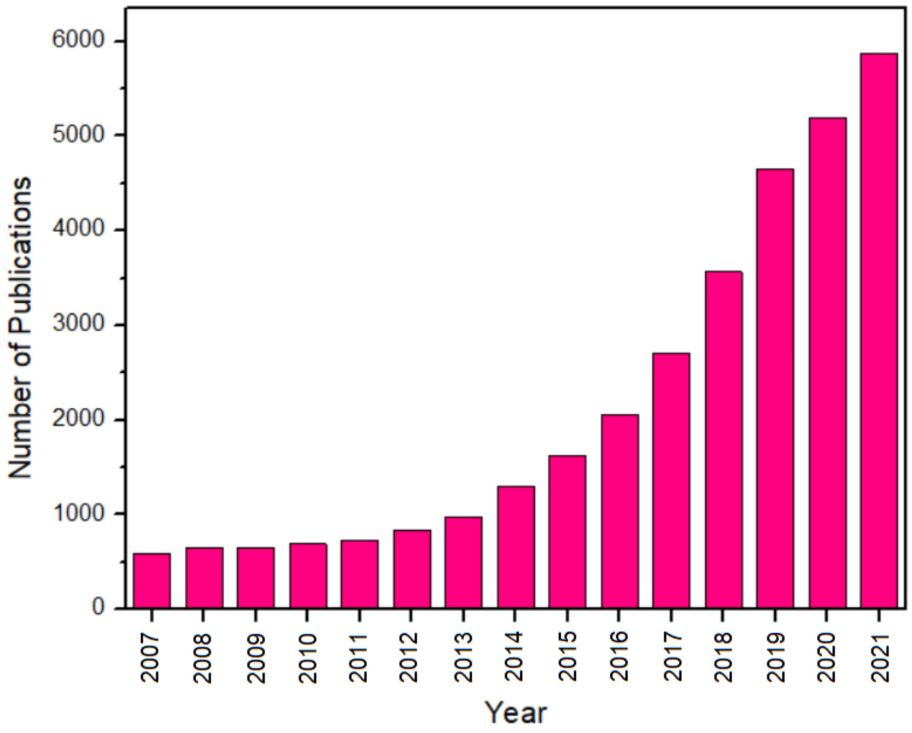

Figure 2. The number of publications using "carbon nitride*" or "g-C_3N_4*" as the topic keywords in the past 15 years. Adapted from ISI Web of Science (WoS) (date of search: 16 March 2022).

GCN Properties and Modification Method

The photoactivity of GCN was discovered by Wang et al. in 2009, and the author showed that GCN can generate hydrogen (H_2) under visible light [27]. The bandgap of GCN is 2.7 eV, which is a solar active photocatalyst that can absorb light wavelengths up to 460 nm [28]. It results from the sp^2 hybridization of the nitrogen and carbon that form the π-conjugated graphitic planes with comparable graphite structures [29]. The materials with delocalized conjugated π-structures have been confirmed to demonstrate a low rate of charge recombination due to high electron–hole separation efficiency. GCN consists of carbon and nitrogen, which is an abundant photocatalyst that can be synthesized by a simple method, such as thermal polymerization. Most importantly, it is metal-free. The GCN layered structure is similar to graphite due to the interlayers being held by van der Waals forces. It was noticed that GCN consists of seven phases; however, only g-h-triazine and g-h-heptazine exhibited its photoactivity [30]. In other words, there are two different condensation states demonstrated on the GCN networks, which are (i) heptazine/tri-s-triazine units (Figure 3a) and (ii) s-triazine units (Figure 3b).

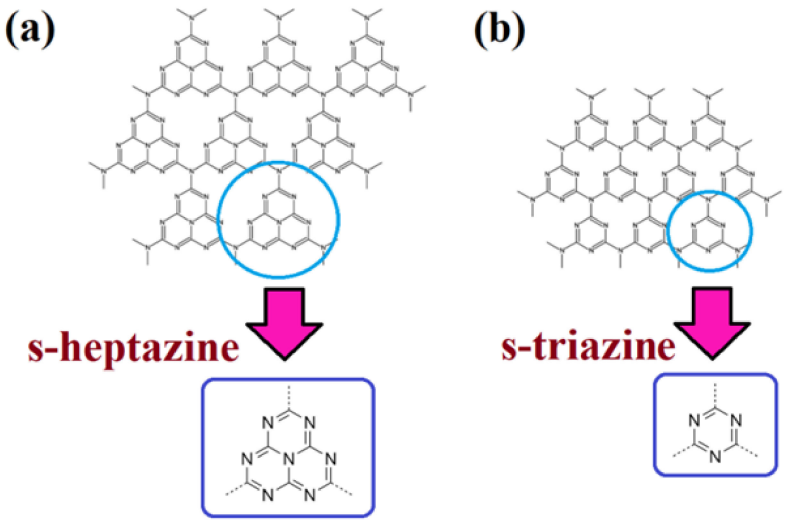

Figure 3. The structures of (**a**) s-heptazine; and (**b**) s-triazine unit. Reproduced with permission from Ref. [31].

The most widely used method was the high-temperature pyrolysis of nitrogen-rich organic species such as urea, dicyandiamide, and cyanamide, which was seen as a good synthetic strategy for generating the least defective polymeric species. Figure 4 shows a proposed GCN formation pathway with the starting material of cyanamide. In the first step, the reaction is a mixture of polyaddition and polycondensation process where the cyanamide is condensing to become melamine. In the pyrolysis procedure, when the pyrolysis temperature achieved 350 °C, essentially melamine-based products are formed, while the heptazine forms via melamine rearrangements at approximately 390 °C. Intermediate products including melam, melem, and melon will be generated during the thermal condensation [32]. When the temperature increases to 520 °C, condensation of this unit to polymers, networks, and potentially the final polymeric carbon nitride occurs. A thermal gravimetric analysis (TGA) was conducted by scientists, and it was reported that the stability of GCN is up to 600 °C [33]. GCN can be fully broken down at 700–750 °C. Particularly, GCN has the highest thermal stability among organic matter. The high thermal stability of GCN was featured in various applications such as heterogeneous catalysis. It can also be used as a template and structuring agent because it allows a simple removing process by increasing the heating temperature to 600 °C and above.

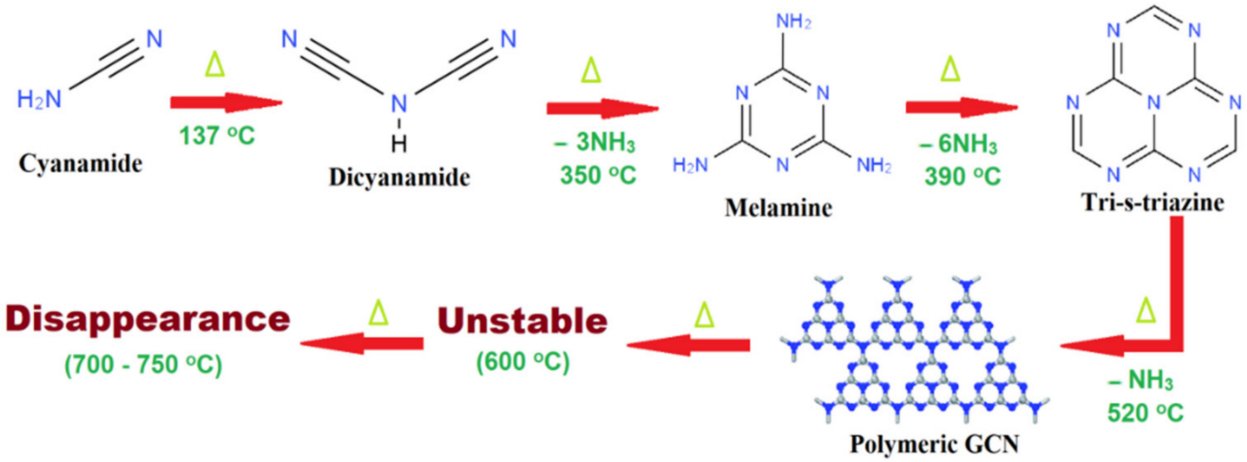

Figure 4. Reaction pathway to form GCN by using cyanamide as starting material. Adapted from Ref. [34].

As mentioned above, GCN is a potential material for photocatalysis, but a pristine GCN possesses limitations, for instance (i) small surface area, (ii) high recombination rate, and (iii) low absorption of visible light. Therefore, several initiatives were taken to improve the GCN photocatalyst. Generally, there are four ways to modify GCN, which are doping, exfoliation, self-heterojunction, and composition (Figure 5).

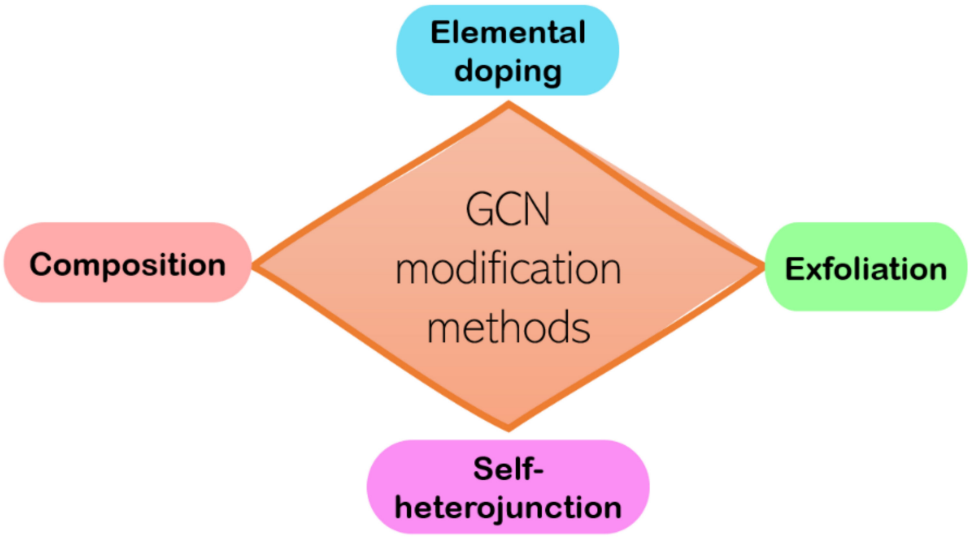

Figure 5. A summary of the GCN modification methods.

The surface area of pristine GCN reported is low (5–10 m^2/g), which is not beneficial for photocatalysis reaction [35]. Exfoliation can be chemical exfoliation or thermal exfoliation; it is a method to delaminate the GCN interlayer and obtain a higher surface area. For example, chemical exfoliation by introducing ascorbic acid to the precursor of GCN can improve the surface area from 5.54 to 193.98 m^2/g. This is because the ascorbic acid helps to exfoliate GCN by forming pores, creating extra active sites for the photoreaction [36]. Meanwhile, thermal exfoliated GCN managed to increase the surface area from 9.64 to 127.53 m^2/g [37]. Papailias et al. mentioned that chemical exfoliation would be more beneficial for photocatalysis; that is, due to chemical-exfoliated GCN showing lower thickness than thermal exfoliation GCN, the low thickness of GCN has more interfacial contact of target pollutant [37]. However, the exfoliation method can cause blue shifting in light absorption due to the quantum confinement effect (QCE), resulting in less solar photoactivity [37].

The high rate of photogenerated charge recombination can weaken photoactivity. Thus, composition and self-heterojunction are generally used. It is a method by combining two different photocatalysts to form an interface between the composites. When the reaction takes place, the interfacial barrier is modulated, which has a direct effect on the charge transfer characteristics of the heterojunction. The composites generally use two or more different photocatalysts to form heterojunctions, such as WO_3/GCN [38], MoO_3/GCN [39], and GCN/$CdWO_4$ [40]. Self-heterojunction is a band alignment strategy that was ameliorated by fabricating isotype heterojunction by using the same material with different phases, for example, anatase-TiO_2/rutile-TiO_2 [41] and α-Bi_2O_3/β-Bi_2O_3 [42]. The GCN bandgap can flexibly adjust in the range of 2.4 to 2.8 eV by using various preparation methods and starting materials. So, researchers attempted to form a heterojunction with dicyandiamide synthesized GCN (GCN-D) and melamine (GCN-M) synthesized GCN. Based on Figure 6, an electron from GCN-M is transferred to GCN-D, causing electron–hole separation and prolonged charge carrier lifespan [43]. The major drawback of this modification method is poor redox performance [44] and difficulty to maintain long-term stability due to pH-sensitivity [45] in a certain type of heterojunction such as Z-scheme and Type II heterojunction.

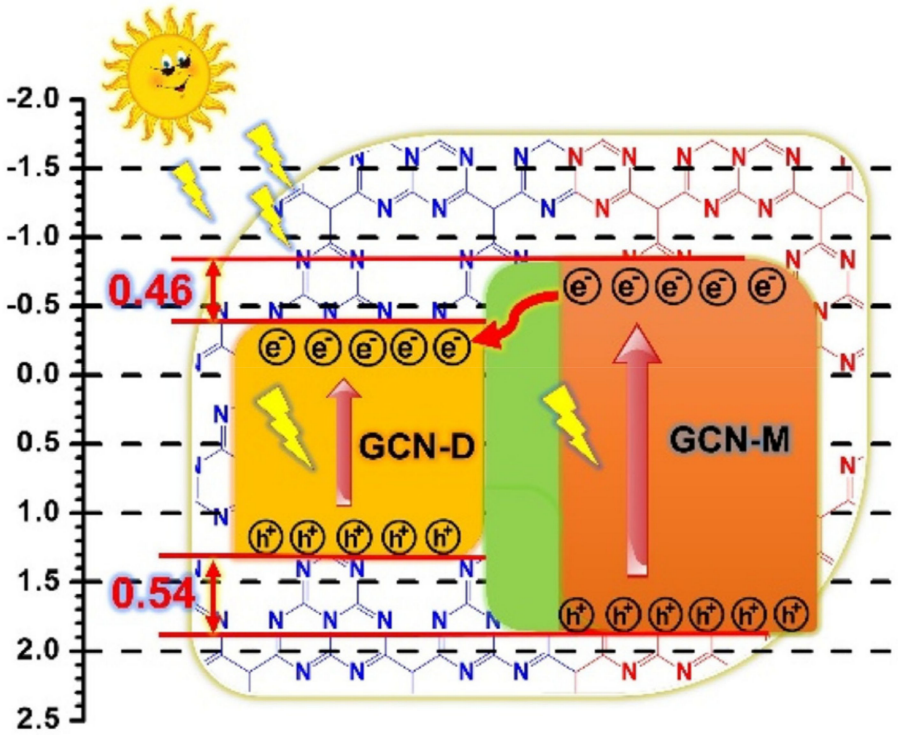

Figure 6. Mechanism of self-heterojunction GCN. Reproduced with permission from Ref. [43].

Limited light absorption is one of the popular issues for most photocatalysts; it can directly affect the photocatalysis process. When the light absorption is low, the bandgap is wide and vice versa. Bandgap engineering is a technique to modify the bandgap of the semiconductor photocatalyst. Doping is a common technique to tune the bandgap energy of the photocatalyst by introducing a small amount of foreign elements into the photocatalyst. Most pure photocatalysts consist of some drawbacks that limit their photocatalytic efficiency; doping is one of the important techniques to improve the photocatalytic performance by enhancing its characteristics. Doping can improve the photocatalyst by (i) extending the light absorption to the visible light region by narrowing the bandgap, (ii) suppressing the charge recombination rate to promote more charges to perform photocatalytic reaction on the photocatalyst surface, and (iii) enhancing the surface area of the photocatalyst. For example, Panneri et al. reported that C-self-doped GCN can alter

the bandgap value from 2.80 to 2.54 eV. This is because the bridging N atom has been substituted by a C atom, and delocalization improved to impede the electron–hole recombination [46]. Doping not only narrows the bandgap energy but also increases the surface area and suppresses the recombination rate at the same time. For instance, F-doped GCN helps to reduce the charge recombination rate due to the electron-withdrawing ability, and the strong electronegativity of F can prevent recombination [47]. B-doped GCN improved the surface area from 39.5 to 55.0 m^2/g by adding boric acid as a dopant. This is due to the decomposition of boric acid at high temperatures, forming pores by releasing gas from the reactant [48]. In summary, doping is a great modification method to improve the low surface area, low light absorption, and recombination issues. The recent advances in single-doped GCN have been reviewed earlier by other researchers [25,49]. Multi-elemental doping can provide better performance in photocatalytic reactions due to the synergetic effect between dopants. Thus, the following section will discuss critically co-doped, tri-doped, and rare-earth-doped GCN.

2. Multi-Elemental and Rare-Earth Element Doped GCN

There are various kinds of elements that have been reported by researchers to dope with GCN photocatalysts for different kinds of applications. This section consists of four sub-sections, namely metal-based co-doping, non-metal-based co-doping, tri-doping, and rare-earth-doping.

2.1. Metal-Based Co-Doping

Elemental doping has been developed to greatly improved the photocatalytic property of GCN. These doping could produce additional binding, form a new band, enhance the photocatalytic performance, and adjust the energy band structure [23]. In recent years, researchers have been switching their focus on co-doping GCN, which provides enhanced photocatalytic activity. There are two types of co-doping of metal elements: (i) metal/non-metal synergy and (ii) metal/metal synergy.

2.1.1. Metal/Non-Metal Synergy

Doping is not only introducing foreign elements to the GCN structure. However, it may also form some functional groups in the GCN structure. Zhu et al. reported that K, F co-doping contributed three changes to the GCN structure, which are (i) K junction in between interlayers, (ii) formation of C-F bond, and (iii) formation of C≡N triple bond. The authors reported that intercalating K in between GCN interlayers can produce an internal electric field in the GCN structure, which can boost the electron transfer of the interlayer, and therefore, the charge recombination is retarded. As a result, these three criteria have enhanced the photocatalytic performance of GCN. The H_2 production by using K, F-GCN (1039 μmol g^{-1} h^{-1}) was 8.5 times better than pristine GCN (122 μmol g^{-1} h^{-1}) [50]. Apart from that, Jing et al. reported that K doping can donate charges to the GCN structure and therefore induce upshifting of the Fermi level to CB minimum (CBM) [51]. Furthermore, the C-F bond possesses a more stable and stronger bonding than C-Cl, C-Br, and C-I due to the atomic radius factor due to its better ionic character. It was proposed that the doping of K will be located near N due to the high electronegativity. As shown in Figure 7, the K dopant will break the $C_{2N\text{-}NHx}$ bond and combine with the residual N atom, leaving the $C_{2N\text{-}NHx}$ to form C≡N groups at the melon structure of K-co-doped GCN [51]. Meanwhile, the C≡N group can act as an electron acceptor in the GCN structure. Thus, the high electronegativity of F and good electron acceptor of C≡N can promote efficient charge carrier separation. This has narrowed the bandgap of GCN from 2.71 to 2.67 eV, which allows better visible light absorption. It was reported by another research team that halogen always contributes more to bandgap narrowing compared to alkali metals [52]. This is because halogens such as F and I can create mid-gap states. Guo et al. synthesized uniform mesoporous K, I-GCN with the SBA-15 template. Initially, K, I-GCN has caused a bathochromic shift in light absorption, which is good for photocatalytic activity. Figure 8a

shows the K, I-GCN structure, proposing that I is substituted to the N position, while K is placed at the interstitial GCN structure. Mesoporous K, I-GCN can cause a hypsochromic shift to light absorption, in which the bandgap value was 2.80 eV, which is slightly larger than pure GCN (2.78 eV). However, the mean lifetime of mesoporous K, I-GCN (5.79 ns) was longer than pure GCN (2.13 ns) and K, I-GCN (5.14 ns). Figure 8b shows the PL spectra of K, I-GCN, in which the peak intensity was greatly reduced compared to pure GCN. The long lifetime of mesoporous K, I-GCN is mainly due to the uniform structure of mesoporous K, I-GCN that exhibits less resistance for electron transportation, causing fast transport of electrons and thus promoting high charge separation. Therefore, the H_2 production of mesoporous K, I-GCN (80.58 μmol h^{-1}) was 9.7 times better than that of pure GCN (8.3 μmol h^{-1}) [52].

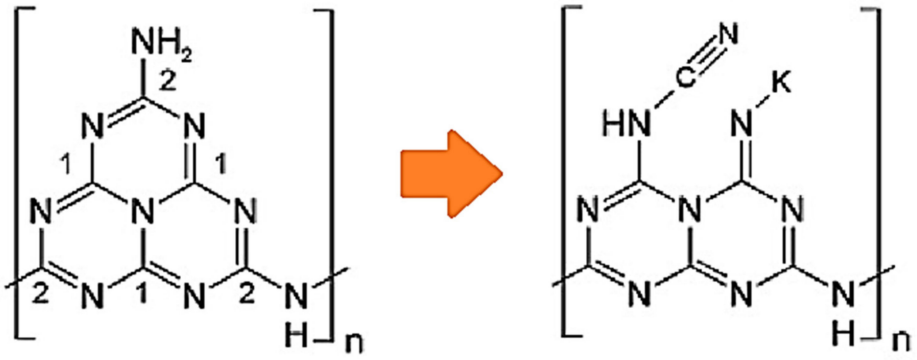

Figure 7. The proposed melon structure changes due to K doping. Reproduced with permission from Ref. [51].

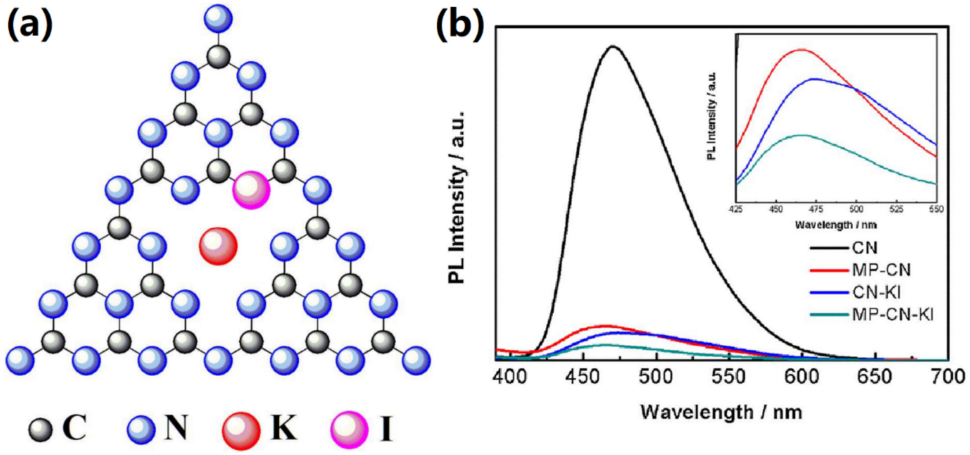

Figure 8. (**a**) The proposed structure of K, I-GCN, and (**b**) PL spectra of pure GCN, mesoporous GCN, K, I-GCN, and mesoporous K, I-GCN. Reproduced with permission from Ref. [52].

It was reported that S-doped GCN is able to cause the reduction in crystallinity due to the incomplete GCN polymerization and numerous H-bonds leaving the GCN intralayer, which potentially obstructs the charge transport in the 2D plane and reduces the GCN photoactivity [53]. To solve this problem, Chen's research team synthesized K, S-GCN using the molten-salt method. It was found that molten-salt synthesized GCN has narrowed the interlayer distance of GCN and thus increased its crystallinity. High crystallinity with dense packing of GCN can allow fast electron transportation on the photocatalyst surface to undergo a reduction with water and produce H_2. Surprisingly, the H_2 production of K, S-GCN (8.78 mmol g^{-1} h^{-1}) was 98 times better than that of pure GCN (0.09 mmol g^{-1} h^{-1}). The improved photoactivity of K, S-GCN is also attributed to the introduction of S. It is because the introduction of S can form a mid-gap state that hinders the recombination rate by trapping the excited electrons temporarily [54]. Another research group mentioned that

the role of K was not significant in enhancing light absorption in K, S-GCN. However, the introduction of K can cause structural bending of the GCN layer (Figure 9a). This is because of interatomic interactions between N, S, and K in the GCN structure, causing N from GCN to move toward K^+. As shown in Figure 9b, the N1 position is the center that is connected to each of the heptazine structures. It was reported that the high charge recombination of pure GCN is due to both the lowest unoccupied molecular orbital (LUMO) and highest occupied molecular orbital (HOMO) not being distributed at the N1 position of GCN, causing the electron transport of the N1 to be obstructed. This finding is in concordance with another research group that studies density functional theory on Pt, P-GCN [55]. Nonetheless, the doping of K, S to GCN has resulted in LUMO and HOMO distributed in the N1 position, which allowed the charges to transfer to neighboring heptazine. In other words, K, S-GCN has improved the charge separation efficiency [56]. On top of that, the doping of K, S to GCN has reduced the bandgap value of GCN, which is beneficial for photoactivity. The VB maximum (VBM) of K, S-GCN has shifted to a more positive level compared to pure GCN, which means that more driving force is allowed for oxidation. Meanwhile, the CBM of K, S-GCN has moved to a more positive level, but the H_2 production capacity has remained. According to Mulliken electronegativity, the shifting of CBM is mainly due to S having weaker electronegativity than N [57]. Na, S-GCN conducted by Chen et al. reported that Na has caused the shifting of VB to a positive position, which allows more driving force for the oxidation reaction. That is because Na atoms that are sandwiched in between two GCN interlayers can donate the outer valence electron (VE) by forming ionic bonds with N. This can change the electron density of the GCN plane. Furthermore, the author found that the type of co-catalyst for water splitting is important. PtCo bimetallic co-catalyst incorporated with Na, S-GCN has extended visible light absorption compared to Pt co-catalyst. This is because the PtCo band structure and electron density can lower the Fermi level of Na, S-GCN and push the excited electrons from Na, S-GCN to transfer rapidly to PtCo, which can facilitate better efficiency in electron–holes separation. Thus, the H_2 generation performance of PtCo/Na, S-GCN (254.7 μmol h^{-1}) was 1.5 times faster than Pt/Na, S-GCN.

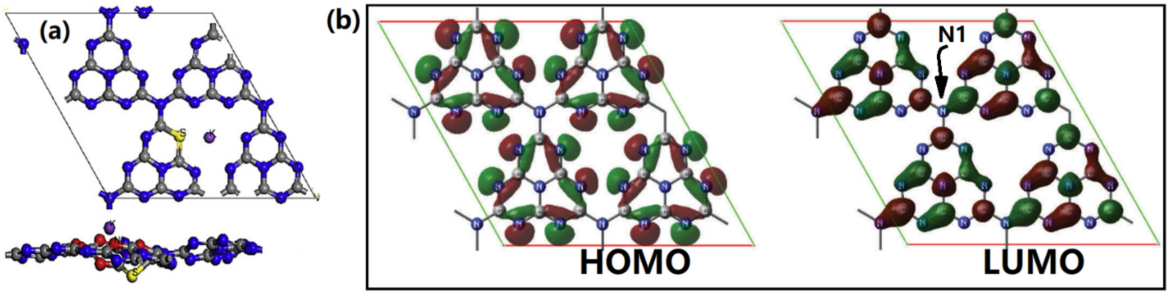

Figure 9. (**a**) The top and side views of bending K, S-GCN, and (**b**) the frontier molecular orbital of the pure GCN layer. Reproduce with permission from Ref. [56].

The Na, S-GCN produced 173.7 μmol h^{-1} of H_2, which was 14 times more excellent than pure GCN (12.4 μmol h^{-1}). Therefore, this has concluded that both GCN dopants and the choice for co-catalyst are the bottom line for photocatalytic water splitting. Li et al. reported that Mo, S-GCN can promote better performance in water splitting. As seen in Figure 10, the way of metal (Mo) binding to GCN structure was slightly different from alkali metals such as Na and K. Instead of only interacting with the N atom, Mo from Mo, S-GCN has bound to the S and N atoms to form a S-Mo bond and N-Mo bond, respectively. Since Mo and S have bound directly and bond tightly to C and N in the GCN structure, it is possible to shorten and fasten the electron transportation pathway, and therefore, the electron can migrate easily on the photocatalyst surface for photocatalytic water splitting. According to the author, the S-Mo group is the active site for H_2 production because the position of S-Mo can act as a trap for photo-excited electrons. Meanwhile, water can simply

be attracted by Mo due to the nucleophile characteristic. It was found that Mo, S-GCN produced 294 μmol g^{-1} h^{-1} of H_2 under irradiation of visible light, while H_2 production for pure GCN, S-GCN, and Mo-GCN was negligible [58].

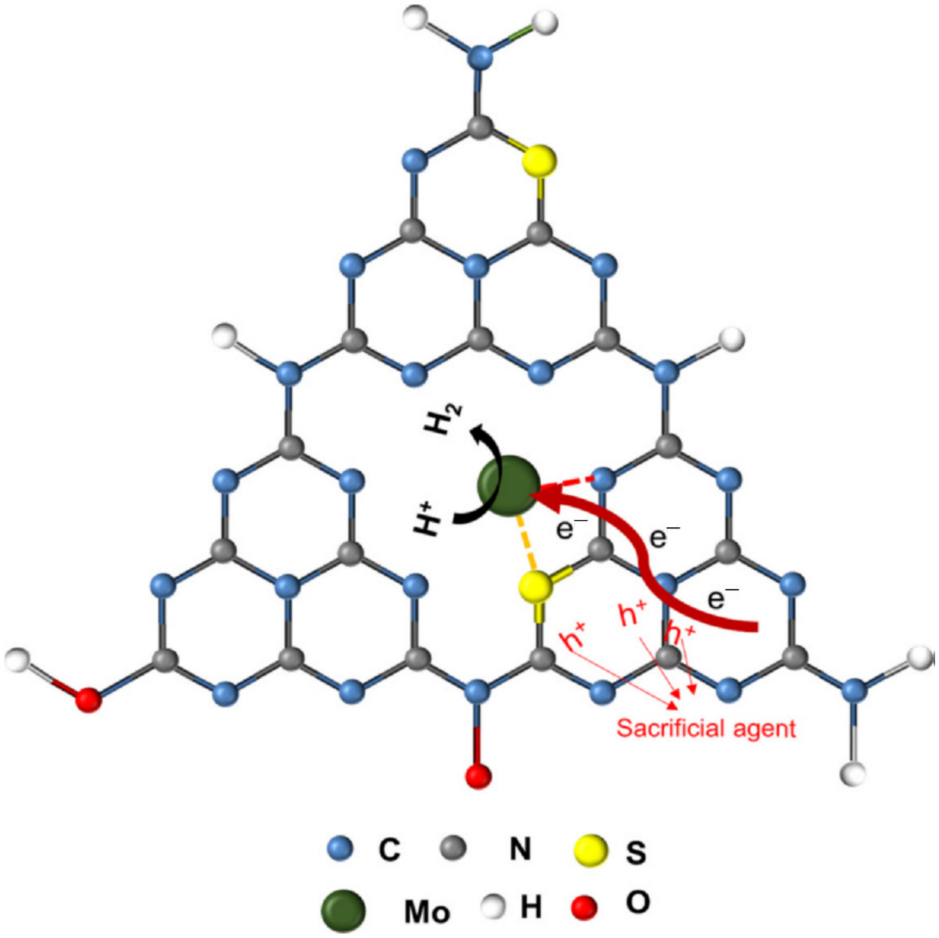

Figure 10. The proposed structure of Mo, S-GCN and the electron pathway for water splitting. Reproduced with permission from Ref. [58].

Fang et al. synthesized Na, O-GCN for water splitting application. As similar to Na, S-GCN, the Na was located at the center of the GCN by forming coordination with neighboring N atoms. It was observed by the author that GCN doped with alkali metals such as K and Na can cause the high electronegativity of the GCN surface at neutral pH, but the author did not elaborate further. Another factor that causes high colloidal stability is the particle size of GCN. A high dispersion GCN is beneficial for some applications such as water splitting and pollutants degradation. Moreover, the bandgap narrowing is mainly due to the O dopant. The O atom that replaced the N site will have extra electrons due to O having more VE. As a result, free electrons from O will then distribute to neighboring C atoms and delocalize in π-bonds; this phenomenon can create a defect state below the CBM, and bandgap narrowing is occurred to promote visible light photoreaction [59]. Meanwhile, K, O-GCN prepared by Lu et al. indicated that O doping can increase the hydrophilic properties of GCN (Figure 11). Initially, the contact angle of pure GCN was 59.5°, but the contact angle of K, O-GCN was 30.1° [60]. That is mainly attributed to the O from the GCN structure forming a H-bond easily with water. High hydrophilicity is beneficial for water treatment and water splitting applications because it can enhance the surface reaction. As a result, the tetracycline (TC) photodegradation by using Ag deposited K, O 0.0259 min^{-1}, which was up to five times more rapid than pure GCN (0.0052 min^{-1}). The purpose of Ag loading is due to the plasmonic effect, which involved transferring excited electrons

between a photocatalyst and noble metals to promote better charge separation. A few researchers conducted studies on transition elements incorporated with O-co-doped GCN. She et al. reported on Ti, O-GCN; the author found that the doping of O to GCN can promote n-π^* transition due to the lone pairs electrons from the O atom [61]. Xu et al. prepared Mn, O-GCN for dye removal. It was reported that transition elements with high oxidation numbers such as Mn can act as a trap for photo-excited electrons temporarily. With the charge-quenching ability, the Amido black 10B dye photodegradation was improved 5.45-fold to 0.0267 min^{-1}. That is because the captured electrons will then diffuse on the surface to capture oxygen to produce $O_2^{\bullet -}$ for photodegradation purposes [62]. In addition to transition elements functioning as trapping centers, Wei et al. reported that W and O co-doping can enlarge the GCN surface area. This is because W was coordinated with six N atoms, forming a metallophthalocyanine-like structure. W-N bonds with active N atoms in the aromatic ring can avoid aggregation by breaking the interlayer periodicity of GCN [63]. This may be due to the doping of the W atom into the GCN structure, weakening the van der Waals forces between the interlayers and hence producing a high surface area of W, O-GCN. The high surface area of W, O-GCN generated 403.57 μmol g^{-1} h^{-1} of H_2, which was 2.5 times higher than pure GCN (171.21 μmol h^{-1} g^{-1}).

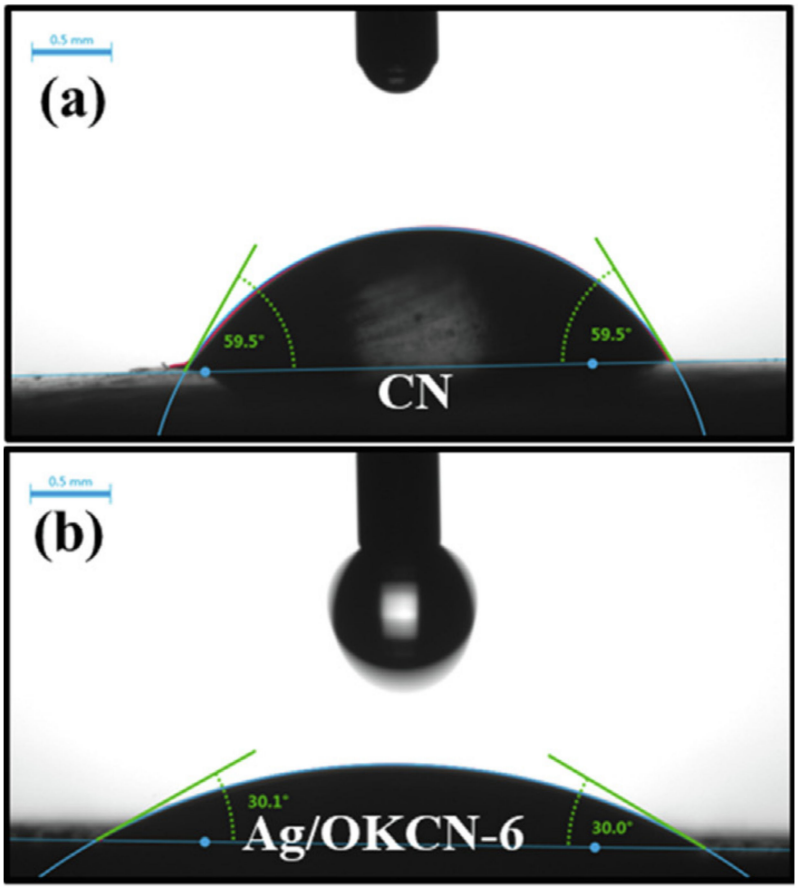

Figure 11. The contact angle of (**a**) pure GCN, and (**b**) Ag deposited K, O-GCN. Reproduced with permission from Ref. [60].

Na, B co-doped GCN was studied by Chi et al., where C atoms in GCN were replaced by B atoms to form the Lewis acid center. Subsequently, Na has formed a N-Na-N bridge in the GCN structure as an electron transfer channel, which accelerates excitation separation and improves the separation efficiency of electron–hole pairs [64]. This finding was in concordance with Ruan et al., who reported on Na, Br-GCN in the first-principles study. The Na from Na, Br-GCN can transfer electrons among two adjacent GCN layers. That is because Na can bind to 4 N, which promotes interlayer charge transfer [65]. Chi et al.

found that the bandgap of Na, B-GCN (2.88 eV) was larger than unmodified GCN (2.78 eV). However, the author mentioned that upshifted CB and downshifted VB has promoted better redox potential and thus enhanced its photodegradation performance. These advantages improve the photocatalytic activity of TC photodegradation with the rate of 0.05 min^{-1}, which was 113 times better than unmodified GCN (0.00044 min^{-1}) [64]. Roselin et al. produced Ag, B-GCN by dissolving boric acid along with melamine followed by calcination. The B-doped GCN was then dispersed with $Ag(NO_3)$ alongside ethanol before calcinating at 400 °C. The Ag, B-GCN resulted in a lower energy bandgap of 2.55 eV as compared to Na, B-GCN due to the presence of Ag producing a surface plasmonic effect to promote better absorption in visible light. It was found that the introduction of Ag has caused band bending to occur at GCN CB, and the Schottky barrier was formed to facilitate charge transfer in one direction, which can avoid charge recombination. This effect combined with the high surface area of co-doping promotes photocatalytic activity. For this material, Rhodamine B (RhB) dye was used for photodegradation. The result shows a significant improvement of photodegradation of 85% in 60 min. The synergetic effect of Ag and B improves the degradation up to 4.2 times as compared to undoped GCN [66]. Wang et al. reported that undoped GCN led to a high charge recombination. That is because the distributions of the HOMO and LUMO were found to have many overlaps based on the modeling study. The doping of K and B into the GCN structure can cause the HOMO and LUMO to be distributed in different regions. Thus, the separation of the electron–hole pairs has accelerated due to the HOMO and LUMO overlapping having been avoided [67].

As shown in Figure 12a, Kundu et al. proposed that the doping of Pt and P can form bridges between two heptazine structures. These two bridges have provided two new electron transportation pathways, C-N-Pt-N-C and C-N-P-N-C, which are beneficial for electron–hole separation [55]. This finding is similar to that of Hu et al., who reported on Fe, P-GCN. The nitride cove of monolayer GCN is 0.71 nm, which is insufficient space for two foreign atoms doped in the same cove. So, both Fe and P were doped at different nitride coves to form Fe-N and P-N bonds to enhance the charge separation efficiency. Generally, the GCN charge transfer is occur by transferring N2p VB to C2p CB. The doping of P has caused the P3p state to be localized below CB, causing bandgap narrowing. The Fe^{2+}/Fe^{3+} (0.77 V vs. NHE) reduction potential is located below GCN CB; thus, the photo-excited charge carrier will be captured by Fe [68]. Meanwhile, the function of Ag dopant in GCN has been discussed earlier; the plasmonic effect will facilitate charge transfer. Nguyen et al. fabricated Ag, P-GCN for sulfamethoxazole (SMX) removal, and it was observed that the pH of the aqueous medium would affect the stability of the photocatalyst. As seen from Figure 12b, the pH_{pzc} of Ag, P-GCN is 6.2, which was unstable in strong acidic pH due to the leaching of Ag. Furthermore, the SMX is anionic when the pH is more than 5.7, but it turns to be cationic when the pH is less than 1.6. Thus, pH 3 is not favorable for SMX removal; the high repulsive force has caused the adsorption of cationic SMX onto the positive charge Ag, while P-GCN is limited. The optimum pH for SMX photodegradation with Ag, P-GCN was pH 9, which was 0.206 min^{-1} and 6.2 times better than pH 3 (0.033 min^{-1}). A gradual decrease in the photodegradation performance in pH 11 was noticed. That is because an inactive layer has formed on the Ag, P-GCN surface. The formation of an inactive layer was due to the nucleophilic OH• attack on the Ag, P-GCN. In addition, there was a repulsion between anionic SMX and negatively charged Ag, P-GCN, which retards the photoactivity [69]. The expensive cost of noble metals such as Ag and Au is still an argument for photocatalyst fabrication. To lower the cost, Chen et al. prepared Eosin Y (EY) sensitized P, Mo-GCN. It was reported that EY can be excited to EY1* by absorbing light and generating the lowest-lying triplet excited state EY3* through an efficient intersystem crossing. This EY3* can undergo reduction with triethanolamine to form $EY^{-\bullet}$. Then, the electron from $EY^{-\bullet}$ is transferred to CB of P, Mo-GCN, causing electron–holes separation. Therefore, the H_2 yield of EY sensitized P, Mo-GCN has improved from 18 to 118 μmol g^{-1} h^{-1}, which is 6.5 times better than undoped GCN [70].

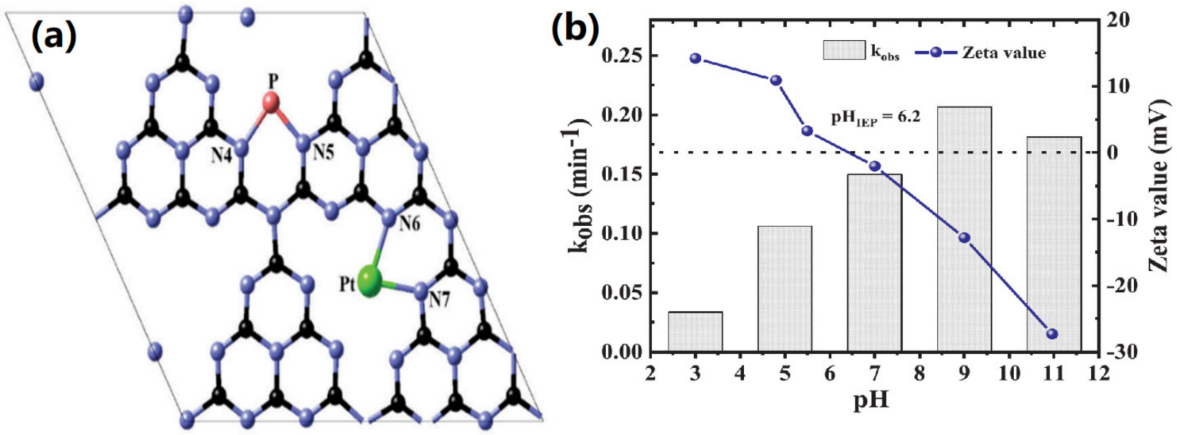

Figure 12. (**a**) The proposed structure of Pt, P-GCN, and (**b**) The SMX photodegradation rate and zeta potential of Ag, P-GCN. Reproduced with permission from Ref. [55].

One of the common issues for metal–non-metal co-doping is that the polymerization and crystal growth is inhibited. Inhibited crystal growth can cause a low crystallinity of GCN, which is not favorable for photocatalytic activity due to the loose structural packing of GCN and increase in defect sites. However, Cao et al. reported that crystal growth inhibition can increase the surface area of GCN. It was found that the enlarged surface area can provide additional spacing for reactants and co-catalyst; in other words, the active site has increased. Figure 13 shows the TEM image of Na, P-GCN that left numerous pores on the surface (11 m^2/g), but no pores were detected on pure GCN (7 m^2/g). The extended surface area and interstitial doping of Na, P-GCN has produced 191 μmol h^{-1} of H_2, which was 2.18 times higher than pure GCN (87.5 μmol h^{-1}). Duan et al. reported the P, Bi-GCN surface area (72 m^2/g) has extended 2.67 times compared to pure GCN (27 m^2/g), and the TC removal performance has improved from 0.0031 min^{-1} to 0.0258 min^{-1} [71]. However, excessive Na and P doping do not improve the photoactivity of Na, P-GCN (66 μmol h^{-1}) but perform lower water-splitting performance than pure GCN [72]. That is mainly due to the excessive dopant such as Na and P acting as a recombination center for the exciting charge. Generally, co-doping with alkali metals such as Na can cause the VB to shift to a more positive level and reduce the driving force for water reduction. The main reason is due to Na donating 3s electrons and forming ionic bonds with N, changing the electron density of the GCN plane and leading to VB shifting [73]. To remove this problem, Yang et al. reported that In, P-GCN does not cause shifting of VB because In5s have contributed to a newly occupied state formed in the VB, which is close to the N2p. The bandgap narrowing is mainly due to the P dopant; as mentioned earlier, P doping can create a defect state below CBM, shifting the CB to a more positive level. As a result, the bandgap of In, P-GCN has lowered from 2.60 to 2.52 eV, which is mainly due to the CB shifting from −1.01 to −0.90 eV [74].

In summary, due to the large atomic radius, most of the metal dopants were placed in the nitride coves of the GCN surface. The role of metal in the GCN structure mainly is to promote better charge carrier separation. Meanwhile, most of the non-metals were replaced with either C/N atoms of a GCN structure or forming a bridge to allow electron transportation. Non-metal does play a major role in shifting the CBM or VBM to narrow the bandgap of GCN. Most of the time, the thermal polymerization of doped GCN can restrain the crystal growth; however, this can be overcome by using molten-salt synthesis. O-based co-doped GCN can enhance the hydrophilicity of GCN, which can promote better performance in photoactivity. Nevertheless, the pH of the reaction aqueous medium does matter; the opposite charges between the photocatalyst surface and medium can form an electrostatic attraction and vice versa. Table 1 shows a summary of the metal-based co-doped GCN. It was found that some of the elements are still yet to be discussed by

researchers for metal/non-metal synergy GCN, for example, Li, Mg, Ca, Cr, and Si-based co-doped GCN.

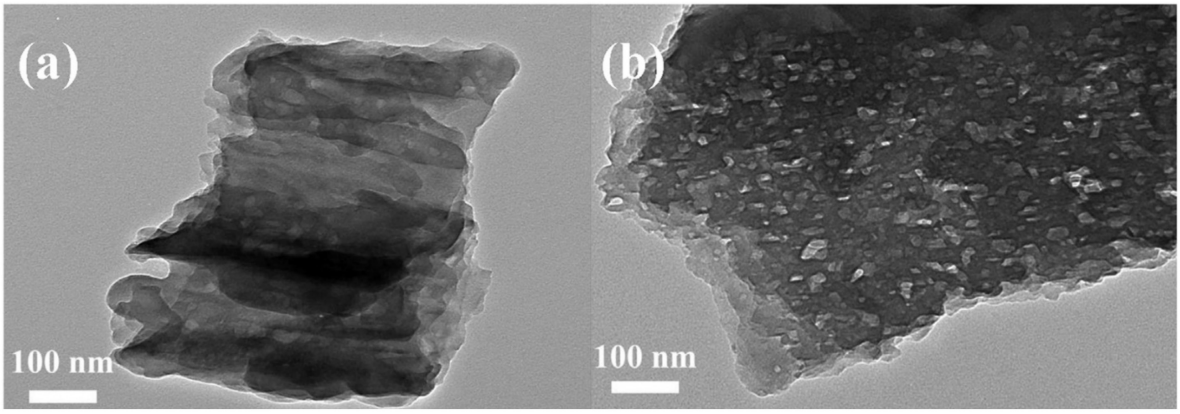

Figure 13. The TEM image of (**a**) pure GCN, and (**b**) porous Na, P-GCN. Reproduced with permission from Ref. [72].

2.1.2. Metal/Metal Synergy

There is not as much study of metal–metal co-doping on GCN as metal–non-metal co-doping. That is mainly because most of the metals are unable to substitute or replace the C and N atoms, which do not contribute much to bandgap modification. Based on Table 1, there are a few researchers who discussed metal–metal co-doping; for example, Bahadoran et al. conducted research on the synergistic effect of Ag and Fe in the GCN structure. It was used in several applications such as photocatalytic, sensors, and antibacterial. However, unlike the Ag, B co-doping mentioned earlier, both Ag and Fe are decorated on the surface of GCN where no atom substitution was reported. This modified GCN can show excellent photodegradation activity of Penicillin G with 99.42% degradation in 25 min because the bandgap has narrowed from 2.78 (pure GCN) to 2.20 eV (Ag, Fe-GCN). Moreover, the electrons from the GCN structure can transfer to Ag and Fe due to energy differences [75]. The author did not discuss the Ag, Fe-GCN structure in depth. However, this could be the plasmonic effect caused by Ag that can allow electrons from GCN to move toward Ag, and the high oxidation number of Fe can temporarily capture electrons from GCN. Apart from Ag, Fe has also been used as a co-doped element together with K as synthesized by Guo et al. In this study, the K forms a bond with C and N; as suggested by the XPS analysis, $K2p_{1/2}$ and $K2p_{3/2}$ correspond to the formation of K-C and K-N bonds, respectively. Meanwhile, the Fe presence in the form of Fe^{2+} and Fe^{3+} ions induces an oxidation state. The combination of these elements as co-dopant causes band alignment downshifts where the VB is moved to a more positive level, causing photogenerated holes with stronger oxidation ability. The co-doped GCN also exhibits p-type behaviors and has a much more positive VB energy, which has a great synergistic effect on the photocatalysis process. The rate constant of RhB photodegradation was 0.0184 mg L^{-1} min^{-1} as compared to pure GCN, which is only 0.0042 mg L^{-1} min^{-1} [76]. K has also been coupled with Zn as a dopant for GCN through thermal polymerization. In this study by Wu et al., the effect of "bridging and bonding" synergy was demonstrated, where induced Zn ions form a bond with nitrogen atoms to produce covalent interactions. This interaction boosted the light-harvesting ability and modified the bandgap from 2.71 (pure GCN) to 2.13 eV (Zn, K-GCN). Meanwhile, the K ions stabilize the structure and constitute efficient ion channels for the transfer of charge carriers between interlayers. The synergy effect was demonstrated in the H_2 production, which was 45.5 times (82.6 μmol h^{-1}) compared to pure GCN (1.8 μmol h^{-1}) [77].

Another bimetallic synergistic effect was also demonstrated using Na and Ca. The Na and Ca were introduced in-plane where the presence of these elements partially destroyed the GCN structure into smaller repeating units forming defects in between, which has caused the surface area to increase from 3.1 m^2/g (pure GCN) to 7.7 m^2/g (Na, Ca-GCN). These structural changes can be illustrated in Figure 14. The bandgap of these modified GCNs decreases from 2.71 (pure GCN) to 2.67 eV (Na, Ca-GCN) due to the alteration of VB and CB as the result of orbital hybridization between C and N atoms and dopant isolated atoms. This property enhances the NO photodegradation by 2.45 times (59.1 μmol g^{-1} h^{-1}) as compared to pristine GCN (23.9 μmol g^{-1} h^{-1}). It was noticed that $CaCO_3$ was detected in XPS, which can cause irreversible chemisorption of the photocatalyst and possibly affect its recyclability [78]. A combination of transition metals has also been studied by Wu et al. on Co and Mo. This study shows that Co and Mo form a bond in the interplanar structure Co–N and Mo–N which is favorable for photocatalytic activity. Interestingly, the presence of Mo in the framework decomposes the GCN and forms mesopores. These mesopores and trapping of electrons by Co and Mo bonds cause a low recombination rate of photogenerated electron–hole pairs, subsequently improving photocatalytic activity. For example, the H_2 evolution (69.45 μmol h^{-1}) and RhB degradation (0.0192 min^{-1}) were 8.6 times and 10.1 times greater than pure GCN (H_2: 8.05 μmol h^{-1}, RhB: 0.193 min^{-1}), respectively. In addition to Mo, Co has also been used to couple with Va. Both Co and V were introduced into in-planes of GCN, resulting in the structural correlation length of interlayer periodicity decreasing. Both Co-N and V-N bonds were detected by XPS, indicating that Co and V were bound to the GCN structure, which promotes good electron delocalization and facilitates photo-excited charge separation. Density functional theory (DFT) suggested that Co and V substituted C1 and C2 positions in the same heptazine structure due to the lowest formation energy, predicting that it is the main structure of Co, V-GCN (Figure 15a). It was noted that there is a limitation to introducing Co/V into the structure, as it may produce new recombination centers to suppress the separation of photogenerated charge carriers. With an optimized amount of Co/V, the modified GCN (0.0108 min^{-1}) can achieve four times higher TC removal efficiency as compared to pure GCN (0.0027 min^{-1}) [79]. Liu et al. studied Fe, Co-GCN, and it was proposed that both Fe and Co atoms be substituted to the N position but in different heptazine structures (Figure 15b). The experimental light absorption of Fe, Co-GCN was the same as the simulation outcome, that the Fe, Co-GCN possess extended light absorption between 450 and 650 nm. This is mainly due to the shallow donor defect of Fe, Co-GCN, that shifted the VB to a less positive level, causing a bathochromic shift [80].

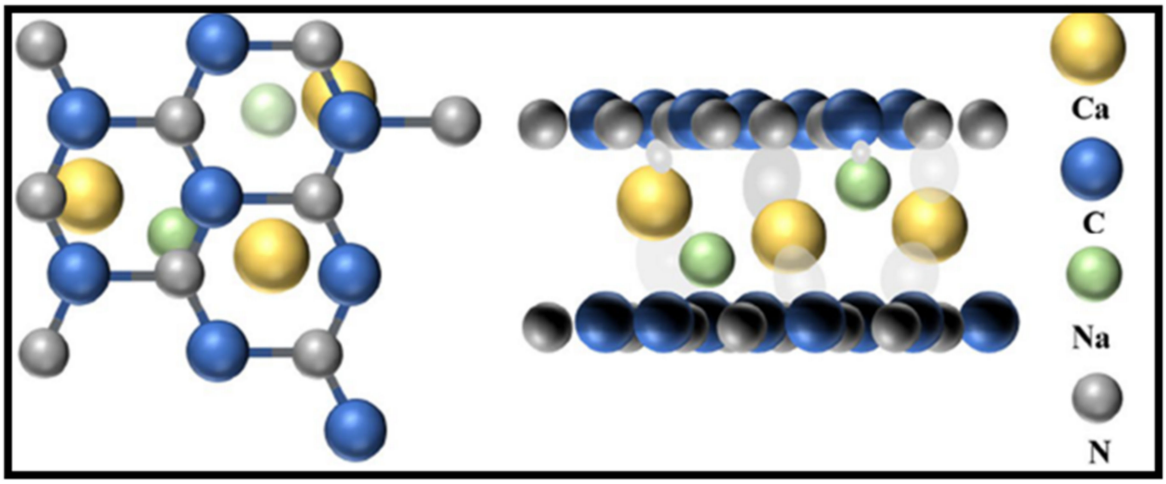

Figure 14. A schematic diagram of Na, Ca-GCN. Reproduced with permission from Ref. [78].

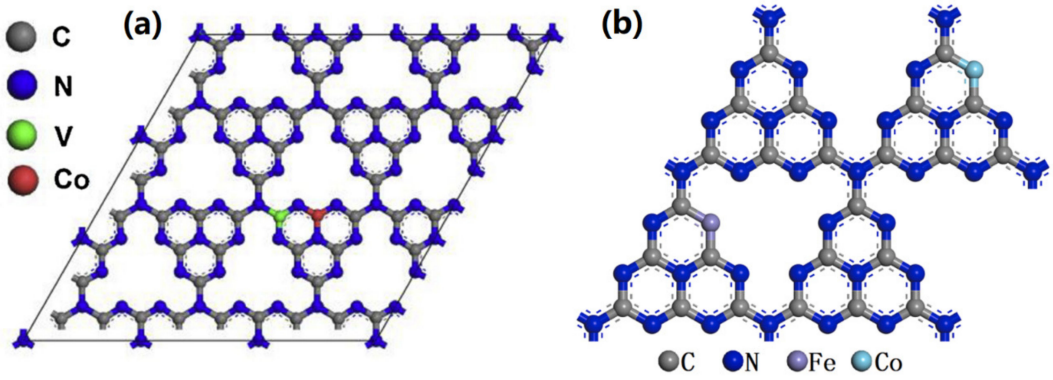

Figure 15. The models of (**a**) Co, V-GCN, and (**b**) Fe, Co-GCN. Reproduced with permission from Ref. [80].

To date, the performance of metal–metal co-doped GCN in photocatalysis is not widely reported. It was found that some metal atoms are substituted for the C or N atoms in the GCN structure, which promote good electron delocalization of the intralayer and alter the band edge. However, some of the metal atoms were loaded in between the interlayers of the GCN structure, which act as a connection between two layers and promote better charge transfer. To sum up, each of the metal elements can play different functions in the GCN structure to enhance the light absorptivity, photoconductivity, and lifetime of photo-excited charges.

Table 1. The summary of metal-based co-doped GCN.

Dopant	Bandgap Energy (eV)	Precursor/ Synthesis Method	Light Source for Reaction	Application	Performance of Activity	Ref. (Year)
Fe, P	2.38	DCDA, diammonium hydrogen phosphate, iron(iii) nitrate nanohydrate/Thermal polymerization 520 °C	250 high-pressure Na lamp	Water splitting	H_2: 150.6 μmol h^{-1}	[68] (2014)
				RhB photodegradation	Rate: 0.0245 min^{-1}	
Na, P	~450 nm	Melamine, sodium tripolyphosphate/Thermal polymerization 550 °C	350 Xe lamp	Water splitting	H_2: 191 μmol h^{-1}	[72] (2017)
Mo, P	2.10	Melamine, ammonium molybdate tetrahydrate, Bis(2-ethylhexyl) phosphate/Thermal polymerization 550 °C	300 W Xe lamp (λ ≥ 420 nm)	Cr (VI) reduction	Rate: 0.0229 min^{-1}	[70] (2019)
				Water splitting	H_2: 118 μmol h^{-1} g^{-1+}	
Bi, P	2.67	Urea, bismuth nitrate pentahydrate, HCCP/Thermal polymerization 500 °C	Stimulated sunlight irradiation (PEC-L11)	TC photodegradation	Rate: 0.02582 min^{-1}	[71] (2019)
Ag, P	2.51	Silver nitrate, urea, phytic acid/Thermal polymerization 550 °C	350 W Xe lamp (λ ≥ 420 nm)	SMX photodegradation	Rate: 0.149 min^{-1}	[69] (2020)
K, P	2.62	DCDA, dipotassium phosphate/Thermal polymerization 550 °C	300 W Xe lamp (λ ≥ 420 nm)	RhB photodegradation	Rate: 0.3126 mg L^{-1} min^{-1}	[81] (2020)
Ba, P (microtubes)	2.52	Melamine, barium chloride, Hypophosphorous acid/Hydrothermal 180 °C, Thermal polymerization 500 °C	500 W Xe lamp (λ ≥ 420 nm)	Water splitting	H_2: 12.3 μmol h^{-1}	[82] (2020)
In, P	2.52	DCDA, dipotassium phosphate, indium chloride/Thermal polymerization 520 °C, Ar	300 W Xe lamp (λ ≥ 420 nm)	Water splitting	H_2: 4.03 mmol h^{-1} g^{-1}	[74] (2021)
Na, B	2.88	Sodium borohydride, melamine/Thermal polymerization 500 °C	350 W Xe lamp (λ ≥ 420 nm)	TC photodegradation	Rate: 0.05 min^{-1} (78.39%, 30 min)	[64] (2022)
Ag, B	2.55	Silver nitrate, urea, phytic acid/Thermal polymerization 550 °C	350 W Xe lamp (λ ≥ 420 nm)	SMX photodegradation	99%, 30 min	[66] (2019)
K, B	2.52	Melamine, boric acid, NaCl-KCl-KBr mixture/Molten-salt 675 °C	300 W Xe lamp (λ ≥ 400 nm)	Water splitting	H_2: 1.18 μmol h^{-1} O_2: 0.58 μmol h^{-1}	[67] (2021)
Na, S	2.77	Sodium bicarbonate, thiourea/Thermal polymerization, 350 °C, 600 °C	300 W Xe lamp	Water splitting	H_2: 173.7 μmol h^{-1}	[73] (2019)
				RhB photodegradation	100%, 30 min	

Table 1. *Cont.*

Dopant	Bandgap Energy (eV)	Precursor/ Synthesis Method	Light Source for Reaction	Application	Performance of Activity	Ref. (Year)
Na, S	2.77	Thiourea, urea, sodium bicarbonate, pluronic F127/Thermal polymerization	300 W Xe lamp ($\lambda \geq 420$ nm)	Water splitting	H_2: 173.7 μmol h^{-1}	[73] (2019)
				RhB photodegradation	Rate: 0.107 min^{-1}	
				p-chlorophenol photodegradation	Rate: 0.011 min^{-1}	
K, S	2.73	LiCl-KCl mixture, trithiocyanuric acid, melamine/Hydrothermal 180 °C, Thermal polymerization 550 °C	300 W Xe lamp ($\lambda \geq 420$ nm)	Water splitting	H_2: 8.78 mmol g^{-1} h^{-1}	[54] (2020)
Mo, S	2.50	Urea, molybdenum(V) chloride, sulfur powder/Thermal polymerization 600 °C	300 W Xe lamp ($\lambda \geq 420$ nm)	Water splitting	H_2: 294 μmol g^{-1} h^{-1}	[58] (2021)
Ni, S	2.44	Nickel nitrate hexahydrate, thiourea, urea/Thermal polymerization 520 °C	350 W Xe lamp ($\lambda \geq 420$ nm)	TC photodegradation	Rate: 0.031 min^{-1}	[83] (2022)
			300 W Xe lamp	CO_2 reduction	CO yield: 58.6 μmol g^{-1} CH_4 yield: 18.9 μmol g^{-1}	
K, O (composite Ag)	2.54	Urea, potassium oxalate monohydrate/Thermal polymerization 520 °C	300 W Xe lamp ($\lambda \geq 420$ nm)	TC photodegradation	Rate: 0.0259 min^{-1}	[60] (2022)
Na, O	2.72	Sodium hydroxide, urea/Thermal polymerization 600 °C, Hydrothermal 160 °C	300 W Xe lamp ($\lambda \geq 400$ nm)	Water splitting	H_2: 45 μmol h^{-1}	[59] (2017)
Mn, O	2.26	Manganese(ii) chloride, formic acid, urea/Thermal polymerization 520 °C	350 W Xe lamp ($\lambda \geq 420$ nm)	MG photodegradation	Rate: 0.0290 min^{-1}	[62] (2020)
				AB10B photodegradation	Rate: 0.0267 min^{-1}	
Ti, O	2.04	Urea, formic acid, titanium tetrachloride/Thermal polymerization 520 °C	300 W Xe lamp ($\lambda \geq 420$ nm)	*E. cloacae* inactivation	6.20 log CFU·mL^{-1}, 60 min	[61] (2021)
W, O	2.57	Ammonium metatungstate, melamine/Thermal polymerization 550 °C	300 W Xe lamp ($\lambda \geq 400$ nm)	Water splitting	H_2: 403.57 μmol g^{-1} h^{-1}	[63] (2021)
Co, O	N/A	Cobalt nitrate hexahydrate, polyvinylpyrrolidone, 2-methylimidazole/Thermal polymerization 600 °C	N/A	OFX degradation	58.1%, 20 min	[84] (2022)
K, I	2.67	Potassium iodide, DCDA/Thermal polymerization 550 °C	300 W Xe lamp ($\lambda \geq 420$ nm)	Water splitting	H_2: 41.23 μmol h^{-1}	[85] (2016)
K, I (mesoporous)	2.80	SBA-15, potassium iodide, DCDA/Thermal polymerization 550 °C	300 W Xe lamp ($\lambda \geq 420$ nm)	Water splitting	H_2: 80.58 μmol h^{-1}	[52] (2018)
K, I	2.65	DCDA, potassium iodide, iodine/Thermal polymerization 550 °C	300 W Xe lamp ($\lambda \geq 420$ nm)	PEC measurement	Photocurrent density: 50.3 μA/cm^2	[51] (2019)
Na, Cl	2.67	DCDA, sodium chloride/Thermal polymerization 550 °C	5 W LED lamp (λ = 420 nm)	RhB photodegradation	97.5%, 50 min	[86] (2019)
				TC photodegradation	66.1%, 60 min	
K, F	2.67	Melamine, potassium fluoride/Thermal polymerization 550 °C	300 W Xe lamp ($\lambda \geq 420$ nm)	Water splitting	H_2: 1039 μmol g^{-1} h^{-1}	[50] (2019)
C, Fe	2.31	DCDA, glucose, iron chloride/Thermal polymerization 600 °C	300 W Xe lamp (λ = 400–700 nm)	RhB photodegradation	Rate: 0.0188 min^{-1}	[87] (2014)
K, Fe	2.69	DCDA, potassium ferricyanide/Thermal polymerization, 550 °C NH_3 atmosphere	300 W Xe lamp ($\lambda \geq 420$ nm)	RhB photodegradation	Rate: 0.0184 mg L^{-1} min^{-1}	[76] (2019)
Co, Mo	2.77	Molybdenum disulfide, guanidine hydrochloride, cobalt (ii) chloride hexahydrate/Thermal polymerization 550 °C	300 W Xe lamp ($\lambda \geq 400$ nm)	RhB photodegradation	94.7%, 15 min	[88] (2019)
Na, Ca	2.67	Sodium chloride, calcium chloride/Thermal polymerization 550 °C	150 W Halogen lamp ($\lambda \geq 400$ nm)	NO oxidation	59.1 μmol g^{-1} h^{-1}	[78] (2020)
Co, V	2.84	Urea, cobalt acetate, vanadyl acetylacetonate/Hydrothermal 150 °C Thermal polymerization 550 °C	250 W Xe lamp ($\lambda \geq 420$ nm)	TC photodegradation	Rate: 0.0108 min^{-1}	[79] (2021)

Table 1. *Cont.*

Dopant	Bandgap Energy (eV)	Precursor/ Synthesis Method	Light Source for Reaction	Application	Performance of Activity	Ref. (Year)
Ag, Fe	2.20	Silver nitrate, iron sulfate heptahydrate/Chemical synthesis	25 W UV lamp (λ = 350 nm)	Penicillin G photodegradation	99.42%, 25 min	[75] (2021)
Zn, K	2.13	Zinc(ii) chloride, potassium chloride/Thermal polymerization 550 °C	300 W Xe lamp ($\lambda \geq$ 420 nm)	Water splitting	H_2:82.6 μmol h^{-1}	[77] (2021)

Remark: N/A: Not available; TC: Tetracycline; RhB: Rhodamine B; SMX: Sulfamethoxazole; HCCP: Hexachlorotriphosphazene; MG: Malachite green; AB10B: Amido black 10B; PEC: Photoelectrochemical; SBA-15: Santa Barbara Amorphous-15; LED: Light-emitting diode; NO: Nitrogenous oxide.

2.2. Non-Metal-Based Co-Doping

The doping of non-metals can form a covalent bond with the GCN structure. This is because non-metals usually have high ionization energy that causes electrons to be held closer by the higher effective nuclear charge. Li et al. studied P, F-co-doped GCN for water-splitting application, and it performed up to 17.8 times better than pristine GCN [89]. Introducing P to the GCN structure can generate a few occupied impurity bands [90]. As a result, P and F in this work have pushed GCN CB to a more negative level and enhanced the driving force for water reduction by producing more H_2. The dopant of P has substituted for the C atom position in the GCN structure. P has an extra VE compared to the C atom. Thus, it can form a negative charge on the GCN surface to increase the adsorption capacity for a reaction. The role of F is to retard the recombination rate by trapping electrons due to F having higher electronegativity and strong electron-withdrawing ability [91]. It was reported that B, F doping caused a structural distortion of GCN. This is because the F was bonded to the C atom in GCN, resulting in the partial conversion of C-sp^2 to C-sp^3. Due to the high electronegativity of F, the B-N bond became longer and led to electrons transfer from heptazine to the F atom, to suppress the charge recombination [92]. P, Cl-co-doped GCN was studied by Yang et al., and it was found that Cl does not improve much in light absorption. XPS shows that the peak of 198.1 and 200.0 eV represents Cl $2p_{3/2}$ and Cl $2p_{1/2}$, respectively (Figure 16b). This denotes that the Cl atom was occupied in the interstitial space of heptazine structure but neither substituted nor formed a new bond with the GCN structure (Figure 16a). Meanwhile, P was substituted in a C atom. Introducing NH_4Cl in the work as a dopant precursor has produced a N vacant in the GCN structure, which can trap electrons and facilitate slow charge recombination, which is beneficial for photocatalysis [93]. In the study, N being vacant may be due to NH_4Cl in the heating process decomposing to ammonia and HCl, weakening the GCN interlayer interactions and leaving N vacant on the surface [94]. Huang et al. synthesized one-dimensional (1D) P, I-GCN successfully by two-step preparation. Initially, P precursor and melamine were used to synthesize GCN by hydrothermal synthesis to form a supramolecular precursor. Then, this supramolecular precursor was then calcined with NH_4I to form the final product. The advantage of 1D photocatalyst is fast electron transport that can prevent charge recombination. The bandgap of P, I-GCN has been narrowed from 2.61 to 2.58 eV. This is because P and I have 5 and 7 VE, respectively, which helped to increase the GCN charge density, causing the HOMO to be shifted to a higher level [95].

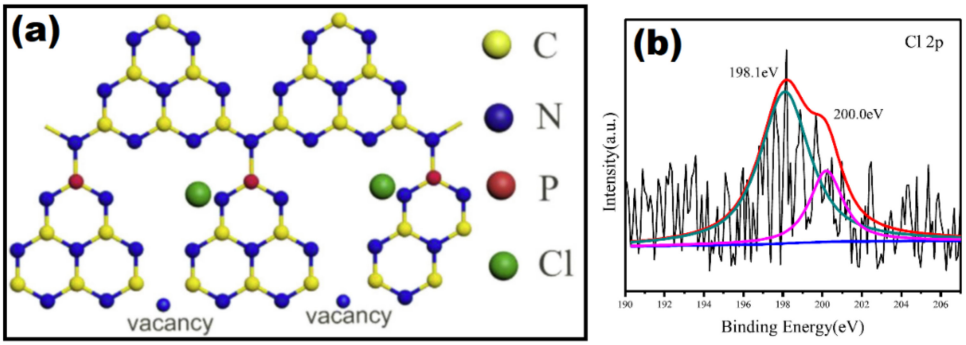

Figure 16. (**a**)The schematic diagram of P, Cl-GCN and (**b**) XPS spectra for Cl 2p. Reproduced with permission from Ref. [93].

Oxygen has been used as a dopant by Huang et al. to form a P, O-GCN using guanidium hydrochloride (GdHCl). In addition to modification, the properties of GCN can also be altered by different precursors. For example, the surface area of GdHCl-produced GCN (65.08 m^2/g) was 3.4 times higher than melamine-prepared GCN. This was mainly because of the drastic decomposition of GdHCl during calcination, which acted as a template for the porous structure, which ends up forming high-porosity GCN [96]. O has replaced N in the GCN structure, so an extra electron from O was delocalized and redistributed to C in the GCN structure. This has led to a defect state that occurred at CBM; as a result, the CB of P, O-GCN (−0.80 eV) has downshifted compared to pristine GCN (−0.83 eV). In addition, the substitution of foreign atoms such as P and O has formed an internal electric field [90]. Pristine GCN is a planar and symmetry structure; the displacement of positive and negative charge in GCN can cause dipole moment, causing the build-up of an electric field and facilitating charge separation [97,98]. As a result, enrofloxacin removal performance with P, O-GCN (0.01 min^{-1}) was 2.6 times better than pristine GCN (0.0038 min^{-1}). A Z-scheme was studied by Huang et al. to combine P, O-GCN and TiO_2, but the light absorption of P, O-GCN/TiO_2 (3.14 eV) was lower than P, O-GCN, which was mainly due to TiO_2 being a less solar-active photocatalyst. P, O-GCN VB (1.77 eV vs. NHE) was not positive enough to allow $^{\bullet}OH$ to be produced ($^{\bullet}OH/OH^-$ = 1.99 eV vs. NHE). So, TiO_2 in the Z-scheme plays a role in oxidizing OH^- to $^{\bullet}OH$ for enrofloxacin removal. Simultaneously, the electron from TiO_2 transferred to P, O-GCN to prevent recombination (Figure 17). The photoactivity was seven times higher than P, O-GCN (0.0695 min^{-1}) and 18.3 times higher than pristine GCN [99].

Hu et al. reported on the P atom from P, S-GCN. It was found that P, S-GCN has made three changes in GCN, which are (i) P has substituted the C position, (ii) S has substituted the N position, and (iii) an interstitial bridge has formed in between two heptazine and linked by a S atom. It was mentioned by the author that pristine GCN consists of a carbon vacancy that can hinder electron transportation. P and S substitutional doping contributed a bathochromic shift to GCN, but interstitial S does not. This is because S only formed a weak covalent bond with both sides of the N atom (N-S-N), which does not change the electronic band of P, S-GCN. However, the interstitial bridge does help to prevent charge recombination. Figure 18 illustrated the doping position of P, S-GCN; it was proposed by the author that charge transfer via N-S-N4-C2-N1-P in the GCN structure has made the photocatalytic activity stronger [100]. Another research group noticed that the structure of P, S-doped GCN was shrunk compared to pristine GCN. This means that the doping of P can inhibit the growth of crystals on GCN and that it is possible to fasten the charge separation [101]. This was also mentioned by Ma et al., that the inhibited crystal growth of P can lead to a high surface area of GCN because of the formation of pores [26]. The methyl orange photodegradation by using P, S-GCN (55.37%) from Jiang et al. was reported to be 7.66 times higher than pristine GCN (7.22%) [101]. Razaida et al. reported a few P, S-GCN nanocomposites to further retard the charge recombination: for example, Type II P, S-GCN/Ag_3VO_4 [102], Z-scheme P, S-GCN/BiOBr/Ag/AgCl [103],

and Z-scheme P, S-GCN/Ag_3PO_4 [104]. According to Raizada et al., a Type II and Z-scheme heterojunction can help to improve photocatalytic activity mainly due to two reasons: (i) charge recombination is retarded due to the charges, which can transfer from photocatalyst I to photocatalyst II or vice versa; (ii) the driving force to produce •OH is enhanced due to Ag-based photocatalyst possessing more positive VB compared to GCN, which can undergo photo-oxidation more efficiently.

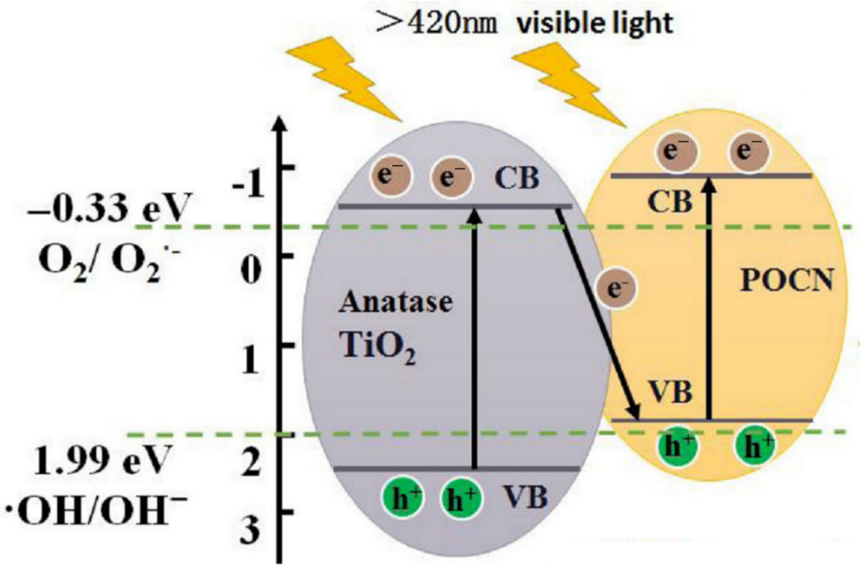

Figure 17. The mechanism of P, O-GCN/TiO_2 photocatalyst under visible light irradiation. Reproduced with permission from Ref. [99].

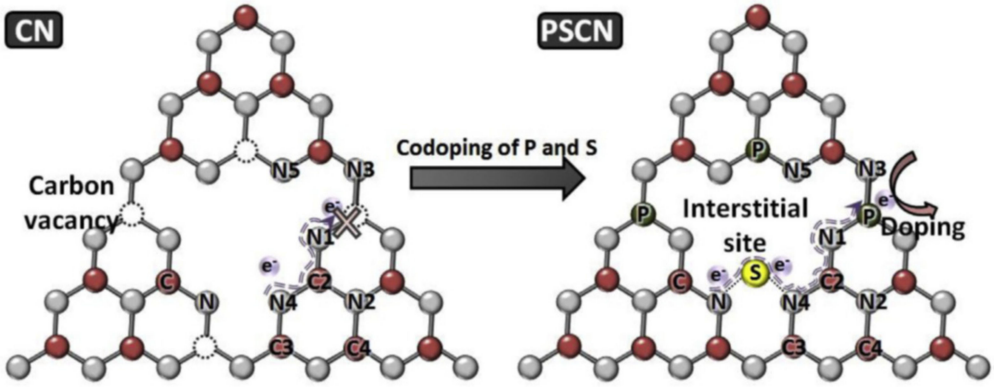

Figure 18. The proposed mechanism of the P, S-GCN charge transfer pathway. Reproduced with permission from Ref. [100].

Zhang et al. found that P, B-GCN can increase the surface area of GCN. The introduction of B increased the GCN surface area to 128.4 m^2/g, because B disrupted the GCN interlayers by increasing the distance between interlayers. P, B-GCN shows a decrease in surface area (61.0 m^2/g), but the author reported that small holes are observed from the FE-SEM image, and it shows that the stacked lamellar was in a loose structure, light-harvesting increased, and the bandgap narrowed, which is beneficial for photoactivity. The triazine photodegradation has ameliorated from 0.0085 min^{-1} (pristine) to 0.0233 min^{-1} (P, B-GCN). This is because the VBM has been shifted to a less positive value and therefore narrowed the bandgap [105]. It was found that B has replaced the C position in GCN. Compared with other anions, B is an electron-deficient element that has only 3 VE; thus, it was possible to act as a Lewis acid site and promote photodegradation. Dong et al. synthesized P, B-GCN nanosheets to further enhance their surface area. P, B-GCN nanosheets were synthesized by the re-calcination of P, B-GCN. It was found that the P, B-GCN nanosheets (85.6 m^2/g)

had a surface area that was 6.7 times higher than P, B-GCN (12.7 m^2/g) [106]. Recalcination of P, B-GCN can lead to mass loss by releasing ammonia gas. This caused the P, B-GCN sheets to be dispersed and therefore the surface area to be enlarged, which is beneficial for its photodegradation behavior [3].

Du et al. reported that the bandgap of O-GCN (2.94 eV) was wider than pristine GCN (2.53 eV). The reason that caused the wide O-GCN bandgap is due to (i) the CB having moved to a more negative value, due to the CBM having shifted, and (ii) the exfoliation process. The author has exfoliated O-GCN (142.80 m^2/g) due to the low surface area of pristine GCN (15.54 m^2/g). QCE is the main reason that caused exfoliated GCN to possess a wide bandgap due to the smaller size of GCN produced by exfoliation [35,107]. Interestingly, the GCN in this study underwent a freeze-drying process before exfoliation. The authors believe that the rapid sublimation of GCN with the freeze-drying method can produce a more porous structure. The introduction of B has further increased the B, O-GCN surface area. The water volatilization temperature is in a similar region to the boric acid decomposition temperature; because of that, boric acid is suggested to be used as the dopant to increase the porosity of GCN [108]. Apart from that, B also narrowed the bandgap of O-GCN. In other words, the B, O-GCN bandgap has been narrowed to 2.85 eV and increased the surface area to 160.58 m^2/g [109]. In addition to bi-elemental doping, Sun et al. reported on B, cyano-GCN for nitrogen photo-fixation. The cyano group has bonded to the heptazine structure, forming defects in the heptazine structure. Since the cyano group is an electron-withdrawing group, it can undergo the nitrogen photo-fixation process to form ammonia by reducing N_2. Both B and cyano groups are electron acceptors; they can perform electron trapping to enhance the charge separation. In addition, N vacancy was found in the heptazine structure due to the high temperature (600 °C) of GCN synthesis. As a result, the nitrogen photo-fixation performance of B, cyano-GCN (115.53 μmol g^{-1} h^{-1}) was 25.5 times better than pristine GCN (4.53 μmol g^{-1} h^{-1}) [110]. Figure 19 illustrates the location of the B, cyano group and N vacancy in GCN structures.

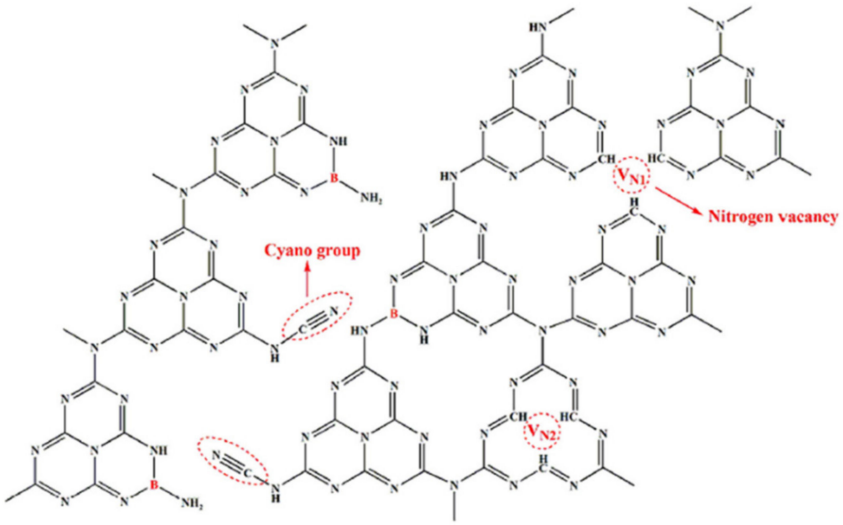

Figure 19. The structure of B, cyano-GCN. Reproduced with permission from Ref. [110].

There are several precursors to dope sulfur into a GCN structure such as thiourea, sulfur, and dibenzyl sulfide. The calcination of thiourea is the easiest method to form S-GCN; it is not only a dopant but also a precursor producing GCN. Babu et al. found that while doping B and S to GCN, B can cause a downshift of CB and an upshift of VB. This is because of S; an extra electron to the neighboring atom caused the π-conjugated network to be reconstructed. VB upshifted is due to the defect states of S being built at the top of the HOMO. It was noticed that the bandgap of B-GCN has slightly broadened compared to pristine GCN; this is because introducing B can cause a restructure of π-VB and π-antibonding CB [111]. A similar finding was found by Han et al. due to the VB

of S, B-GCN being downshifted [112]. Nonetheless, incorporating S in the S, B-GCN can narrow the bandgap due to S being an electron donor in the GCN structure. According to Babu et al., the bandgap has shortened from 2.70 (pristine GCN) to 2.50 eV (S, B-GCN). Interestingly, Mott-Schottky shows that the S, B-GCN is an inverted "v" shape curve, meaning that it has two types of slopes, which are positive and negative (Figure 20a). This indicates that S, B-GCN is a p-n junction photocatalyst, which can accelerate the photocatalytic activity because it can form an electrical potential and direct charges in opposite directions (Figure 20b). As a result, the water splitting of S, B-GCN (53.2 μmol h^{-1}) was eight times more efficient than pristine GCN (6.6 μmol h^{-1}) [113]. Apart from the bandgap, radical active species play a significant role in photodegradation. Yi et al. found that the bandgap S, Cl-GCN (2.55 eV) has successfully narrowed 0.11 eV compared to pristine GCN. The Cl in this study formed a new bond with C in the GCN structure, while S was replaced with N. Thus, Cl is located in between the interlayer of GCN. The Cl 3p orbital can act as an electron acceptor by receiving an excited electron to perform oxidation. Initially, the VB was positioned at 1.86 eV, which is unallowed in $^{\bullet}OH$ production ($^{\bullet}OH/OH^{-}$ = 1.99 eV vs. NHE); however, the downshifted S, Cl-VB was 2.14 eV, and the CB was −0.41 eV. The O_2 oxidation to $O_2^{-\bullet}$ is −0.33 eV vs. NHE. So, this signifies that S, Cl-GCN can generate $O_2^{-\bullet}$ from O_2 oxidation at CB and produce $^{\bullet}OH$ by reducing OH^{-} at the VB at the same time. As a result, the RhB photodegradation with S, Cl-GCN was up to 0.0859 min^{-1}, which was 12.4 times faster compared to pristine GCN (0.0018 min^{-1}).

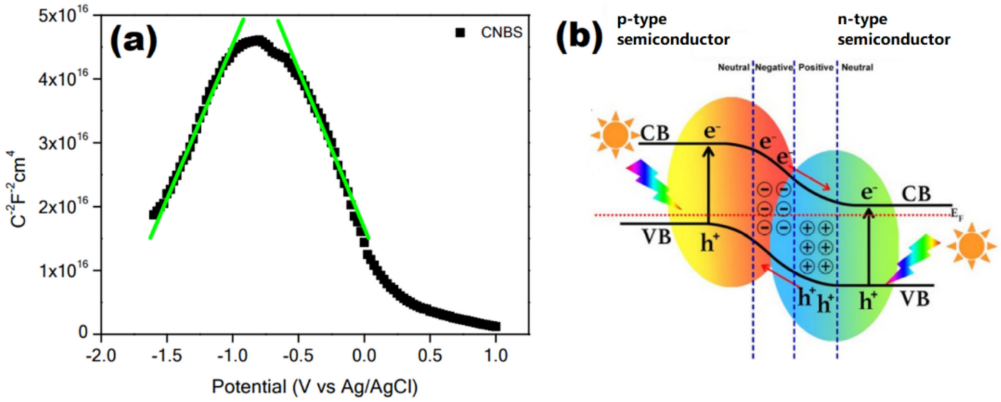

Figure 20. (**a**) The Mott–Schottky graph for S, B-GCN shows 2 slopes, and (**b**) the illustration of the p-n junction. (Reproduced with permission from Ref. [113].)

C, O-doped GCN can promote better electron conductivity and therefore enhanced the charge transfer. The presence of free electrons or polar groups may have a great contribution to electron conductivity. Wu et al. reported that C and O atoms were substituted for the N position in the GCN structure, causing the formation of unpaired electrons by O. This is because N has 5 VE, but O and C have 6 and 4 VE, respectively. Thus, C, O-GCN can act as an electron donor and electron acceptor to promote better charge carrier transfer [114], same as the B, S-GCN, B, P-GCN, and B, O-GCN; it is a donor–acceptor co-doping. So, the bandgap of C, O-GCN has been shortened from 2.78 eV (pristine GCN) to 2.69 eV, and the recombination time of electron–holes pairs was improved by nearly double [115]. Similar findings were found by different researchers; Samanta et al. reported that C, O-GCN enhanced the CO_2 reduction 1.5 times compared to pristine GCN [116]; Jing et al. reported that C, O-GCN was 25.6 times better in bisphenol A photodegradation compared to pristine GCN [117]; Zheng et al. mentioned that C, O-GCN performed nearly six times faster in indomethacin photodegradation compared to pristine GCN [118]. All these are due to the narrow bandgap, the photogenerated electron–hole recombination being suppressed, and the large surface area of C, O-GCN. Cui et al. synthesized C, I-GCN by using dicyandiamide (DCDA). The authors noticed that the surface area of C, I-GCN was small (14.6 m^2/g) but the surface area increased to 54.4 m^2/g after re-calcination.

The recalcination of GCN leads to the hypsochromic shift of porous C, I-GCN, and the bandgap has been widened by 0.06 eV. Nevertheless, the H_2 production of porous C, I-GCN (168.2 μmol h^{-1}) was approximately 10 times better than pristine GCN (17.0 μmol h^{-1}) due to active sites increasing [119].

In summary, unsymmetric GCN allowed n-π* transition, which can enhance light harvesting at visible light [120]. Introducing N vacant, dopant, and 1D nanomaterials can retard the charge recombination and enhance light absorption. S, B-GCN possesses a p-n junction which can facilitate good performance in photocatalysis. P, F-GCN and a N defect in GCN structure are good to suppress charge recombination. Thermal exfoliation is a simple method to enlarge the GCN surface area without using additional chemicals. Table 2 shows a summary of non-metal co-doped GCN reported by different scientists. To date, there has been no report on Br-based co-doped GCN. On top of that, non-metal co-doped GCN is not only for photocatalysis applications but also for non-photocatalytic applications. For instance, Kang et al. synthesized chemical and thermal exfoliated B, N-GCN with a 966.46 m^2/g surface area for Zn-air battery [121]; Piri et al. prepared P, Se-GCN for nitroaromatic reduction [122]. This is because co-doped GCN exhibited some unique properties, for example, good thermal stability, strong chemical stability, and high surface area.

Table 2. The summary of non-metal-based co-doped GCN.

Dopant	Bandgap Energy (eV)	Precursor/ Synthesis Method	Light Source for Reaction	Application	Performance of Activity	Ref. (Year)
P, O	2.51	DCDA, Diammonium hydrogen phosphate/Hydrothermal dissolution–precipitation method 150 °C	250 W high pressure Na lamp (λ = 400–800 nm)	RhB photodegradation	Rate: 0.027 min^{-1}	[26] (2015)
P, O	2.30	Guanidium HCl, PVP, HCCP/ Thermal polymerization 550 °C	350 W Xe lamp (λ ≥ 420 nm)	Enrofloxacin photodegradation	Rate: 0.01 min^{-1}	[90] (2019)
P, O composite anatase TiO_2	2.35	Guanidium HCl, PVP, HCCP/Thermal polymerization 550 °C	350 W Xe lamp (λ ≥ 420 nm)	Enrofloxacin photodegradation	Rate: 0.0695 min^{-1} (98.5%, 60 min)	[99] (2020)
P, S	2.62	HCCP, thiourea/Thermal polymerization 550 °C	300 W Xe lamp (λ ≥ 420 nm)	Methyl orange photodegradation	TOC: 55.37%, 2 h	[101] (2017)
				Tetracycline photodegradation	TOC: 70.33%, 2 h	
P, S	2.68	Melamine, HCCP, sulfur/Thermal polymerization 550 °C	300 W Xe lamp	Methylene blue photodegradation	Rate: 0.048 min^{-1} 100%, 2 h	[100] (2018)
P, S (One-dimensional)	2.83	Dibenzyl sulfide, diammonium phosphate, melamine/Thermal polymerization 650 °C	300 W Xe lamp (λ ≥ 400 nm)	Water splitting	8163.5 μmol g^{-1} h^{-1}	[123] (2019)
				RhB photodegradation	Fully photodegrade, 5 min	
P, S composite Ag_3PO_4	P, S-GCN: 2.51	HCCP, thiourea/Thermal polymerization 530 °C	35 W LED lamp	2, 4 dimethyl photodegradation	Rate: 0.0086 min^{-1}	[104] (2019)
P, S composite Ag_3VO_4	P, S-GCN: 2.51	HCCP, thiourea/Thermal polymerization 520 °C	35 W LED lamp	Phenol photodegradation	Rate: 0.0087 min^{-1}	[102] (2019)
P, S	2.60	Thiourea, thiocyanuric acid, HCCP/Thermal polymerization 550 °C	300 W Xe lamp (λ ≥ 400 nm)	Water splitting	H_2: 1969 μmol g^{-1} h^{-1}	[124] (2020)
P, S composite ZnCr LDH	2.64	Diammonium hydrogen phosphate, sulfur powder, melamine/Thermal polymerization 550 °C	250 W Hg lamp (λ ≥ 420 nm)	Ciprofloxacin photodegradation	95.0%, 90 min	[125] (2020)
			150 W Xe lamp (λ ≥ 420 nm)	Water splitting	H_2: 1319 μmol, 2 h	
P, S composite BiOBr/Ag/AgCl	P, S-GCN: 2.60	Thiourea, ammonium hydrogen phosphate/Thermal polymerization 520 °C	35 W LED lamp	Phenol photodegradation	Rate: 0.0089 min^{-1}	[103] (2020)
P, S with Ag deposited	2.66	Urea, thiourea, phosphoric acid/Thermal polymerization 520 °C	300 W Xe lamp (λ ≥ 420 nm)	*E. coli* inactivation	7.0 log E. coli inactivation, 60 min	[126] (2020)
P, Se	N/A	Melamine, selenium black, HCCP/Thermal polymerization 550 °C	N/A	Reduction in nitroaromatics	99.0% removal, 25 min	[122] (2021)
P, B (Nanosheets)	2.61	1-Butyl-3-methylimidazolium hexafluorophosphate, boric trioxide, melamine/Thermal polymerization 520 °C	300 W Xe lamp (λ ≥ 420 nm)	Oxytetracycline photodegradation	Rate: 0.01 min^{-1}	[106] (2019)

Table 2. *Cont.*

Dopant	Bandgap Energy (eV)	Precursor/ Synthesis Method	Light Source for Reaction	Application	Performance of Activity	Ref. (Year)
P, B (One-dimensional)	2.66	Melamine, phosphoric acid, boric acid/Hydrothermal 170 °C, Thermal polymerization 500 °C	8 × 8 W visible lamps ($\lambda = 460 \pm 40$ nm)	Diclofenac photodegradation	Rate: 0.056 min^{-1} TOC: 62.3%, 90 min	[127] (2021)
P, B	2.63	Boron trioxide, ammonium phosphate dibasic, urea/Thermal polymerization 550 °C	Visible light irradiation ($\lambda \geq 400$ nm)	Atrazine photodegradation	Rate: 0.0233 min^{-1}	[105] (2021)
P, F	2.41	Sodium pyrophosphate, ammonium fluoride, melamine/Thermal polymerization 550 °C	300 W Xe lamp ($\lambda \geq 420$ nm)	Water splitting	H_2: 1690.56 μmol g^{-1}, 6 h	[89] (2021)
P, Cl	2.73	Ammonium chloride, melamine, ammonium phosphate/Thermal polymerization 550 °C	70 W visible light	Norfloxacin photodegradation	Rate: 0.0193 min^{-1}	[93] (2020)
				RhB photodegradation	Rate: 0.047 min^{-1}	
P, I (One-dimensional)	2.58	Melamine, phosphorus acid, ammonium iodide/Hydrothermal 180 °C, thermal polymerization 500 °C	300 W Xe lamp ($\lambda \geq 420$ nm)	Water splitting	H_2: 93.9 μmol h^{-1}	[95] (2017)
C, O	2.45	DCDA, glutathione/Thermal polymerization 520 °C	300 W Xe lamp ($\lambda \geq 420$ nm)	Water splitting	H_2: 18.38 mmol h^{-1} g^{-1}	[115] (2018)
C, O	2.62	2-Methyl imidazole, thiourea, urea/Thermal polymerization 550 °C	300 W Xe lamp	CO_2 reduction	4.18 mmol g^{-1}, 6 h	[116] (2019)
				H_2O_2 production	60.3 μmol H_2O_2 produced in 30 h	
C, O	2.59	Methylammonium iodide, DCDA/Thermal polymerization 550 °C	350 W Xe lamp ($\lambda \geq 420$ nm)	Indomethacin photodegradation	Rate: 0.0391 min^{-1}	[118] (2020)
C, O	1.70	Propanedioic acid, urea/Thermal polymerization 550 °C	Visible light irradiation ($\lambda > 420$ nm)	Bisphenol A photodegradation	Rate: 0.0488 min^{-1} (97.85%, 60 min)	[117] (2021)
				Conversion of toluene	1.02% conversion in 3 h; selectivity 96%; benzaldehyde formation rate: 391 μmol g^{-1} h^{-1}	
C, I	2.81	DCDA, urea, 1-ethyl-3-methyl imidazolium iodide/Thermal polymerization 550 °C	Visible light irradiation ($\lambda > 420$ nm)	Water splitting	H_2: 168.2 μmol h^{-1}	[119] (2018)
S, Cl	2.55	Ammonium chloride, thiourea/Thermal polymerization 550 °C	Xe lamp ($\lambda \geq 400$ nm)	RhB photodegradation	RhB rate: 0.0859 min^{-1} (98.3%, 30 min)	[128] (2020)
				4-NP photodegradation	Rate: 0.0095 min^{-1} (74.0%, 120 min)	
S, Cl composite CdSe-amine	S, Cl-GCN: 2.76	Thiourea, ammonium chloride/Thermal polymerization 550 °C	300 W Xe lamp ($\lambda \geq 420$ nm)	Water splitting	H_2: 18.8 mmol h^{-1} g^{-1}	[129] (2021)
S, B	2.50	Melamine, thiourea, boric acid/Thermal polymerization 550 °C	150 W Xe lamp ($\lambda \geq 420$ nm)	Water splitting	H_2: 53.2 μmol h^{-1}	[113] (2018)
S, B	2.48	Thiourea, melamine, boron trioxide/Thermal polymerization 520 °C	300 W Xe lamp	RhB photodegradation	Rate: 0.0495 min^{-1} (100%, 80 min)	[112] (2018)
B, cyano group	2.54	DCDA, boric acid/Thermal polymerization 600 °C	300 W Xe lamp	Nitrogen photo-fixation	115.53 μmol g^{-1} h^{-1}	[110] (2021)
B, O	2.85	Boric acid, melamine/Thermal polymerization 550 °C	300 W Xe lamp ($\lambda \geq 420$ nm)	Water splitting	H_2: 9751 μmol h^{-1} g^{-1}	[109] (2021)
B, F	2.65	DCDA, N-ethylpyridinium tetrafluoroborate/Thermal polymerization 550 °C	Visible light irradiation ($\lambda > 420$ nm)	Water splitting	H_2: 687 μmol, 2 h	[130] (2018)
B, F	2.72	DCDA, 1-Ethyl-3-methylimidazolium Tetrafluoroborate/Thermal polymerization 550 °C	300 W Xe lamp	Water splitting	H_2: 351 μmol h^{-1}	[131] (2018)
B, N	Surface area: 966.46 m^2 g^{-1}	Pentaerythritol, boric acid, melamine/Thermal polymerization 550 °C, hydrothermal 120 °C	N/A	Zn-air battery	Power density: 193.6 mW cm^{-2}	[121] (2021)

Remark: N/A: Not available; HCl: Hydrochloride; PVP: Polyvinylpyrrolidone; HCCP: Hexachlorotriphosphazene; RhB: Rhodamine B; 4-NP: 4-nitrophenol; PSA: Prostate-specific antigen; PEC: Photoelectrochemical; DCDA: Dicyandiamide; LDH: Layered double hydroxide; CdSe-D: Cadmium Selenide-diethylenetriamine.

2.3. Tri-Doping

Like co-doping, the tri-doping system introduces three different elements in the GCN. The outstanding photoactivity of tri-doped GCN is mainly due to the bathochromic shift of light absorption to promote good photoactivity under sunlight, the formation of defects to facilitate rapid charge transfer, and improved surface functionality. Liu et al. worked on S, P, O-GCN. The outcome has similarity to Hu et al., a group that researched the P, S-GCN and reported that S can form a N-S-N bridge in between two heptazine rings. However, one of the differences between P, S-GCN and S, P, O-GCN is the introduction of an O dopant. Liu et al. reported that an O dopant has replaced the N position in GCN. Compared with Hu's outcome, the extra O in the GCN structure provides an extra two electrons to be excited and transferred under the irradiation of light, resulting in higher photoactivity. As a result, the bandgap of P, S, O-GCN has reduced from 2.4 (pristine GCN) to 2.34 eV. At the same time, the H_2 production was 2479 μmol g^{-1} h^{-1} for S, P, O-GCN, which was 5.3 times better compared to pristine GCN (465 μmol g^{-1} h^{-1}) [132]. Another research group reported that S, P, O in the GCN structure play different roles in photocatalysis [133]. For example, P in GCN localizes the excited charges and acts as active sites for photocatalysis reactions dye to P-induced high charge transfer in the GCN structure. Meanwhile, O and S in GCN contribute to the electrons transfer process at the GCN-conjugated bonds across neighboring heptazine units. Therefore, the synergetic effect of S, P and O can enhance photocatalytic performance [133].

Ma et al. reported on S, Co, O-GCN by hydrothermal post-treatment. It was found that Co and S restrain the crystal growth of GCN, and therefore, the surface area has been increased from 9.1 to 11.9 m^2/g. However, it was mentioned by the author that hydrothermal treatment can change the GCN morphology by lowering down its surface area. For example, Figure 21a shows the pristine GCN in bulk and the large size of the layer structure; introducing S and Co has restrained the crystal growth of GCN. Thus, the size of the layer structure has fragmented into small sizes (Figure 21b). Figure 21c was the S, Co, O-GCN that underwent a hydrothermal process. The morphology of GCN has changed and reassembled into nanoplates and nanorods, but the surface area has decreased to 6.5 m^2/g. Meanwhile, O in the S, Co, O-GCN can promote the hydrophilic properties of GCN and thus increase the adsorption of the hydrophilic dyes such as RhB. It was noticed that S, Co, O-GCN performs slightly higher adsorption in dark reactions. Since the surface area has decreased from 9.1 (pristine GCN) to 6.5 m^2/g (S, Co, O-GCN), the high adsorption of S, Co, O-GCN is not due to the surface area but is due to the hydrophilicity of photocatalyst. On top of that, S, Co, O-GCN can perform fast photodegradation under anoxic conditions. Instead of oxygen aeration of RhB, O from the S, Co, O-GCN itself can act as a trap for electrons to produce $O_2^{-\bullet}$. Then, $O_2^{-\bullet}$ can react with holes to produce H_2O_2 [134].

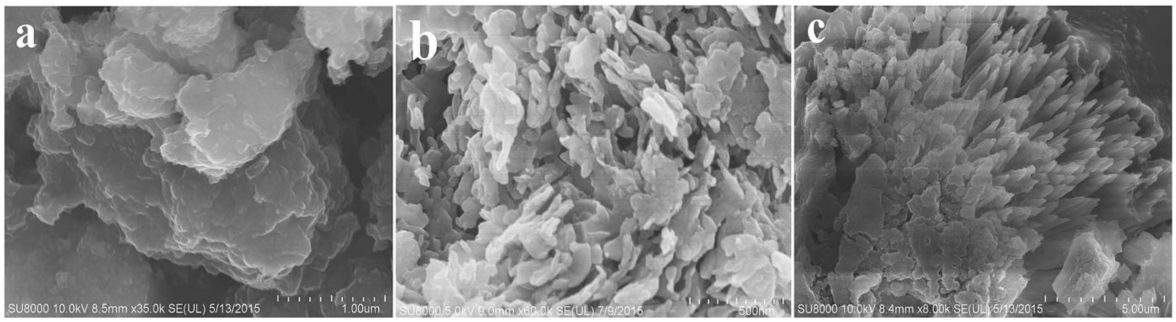

Figure 21. The FESEM micrograph of (**a**) pristine GCN, (**b**) S, Co-GCN, and (**c**) S, Co, O-GCN. Reproduced with permission from Ref. [134].

The summarized literature for tri-doped GCN is shown in Table 3. The amount of literature reporting tri-doped GCN is still small. Nonetheless, a tri-doping system can integrate the benefits of each of the dopants to further enhance the performance in

photocatalysis. For example, Ma et al. reported that introducing S, Co, O to GCN not only can restrain the crystal growth but can also enhance the pollutant adsorption and promote good photodegradation performance in anoxic conditions. As a result, combining different dopants to the GCN structure can solve several limitations of pristine GCN. Apart from photocatalytic applications, Wu et al. synthesized Fe, Co, O-GCN for tetracycline degradation with persulfate activation. This is because Fe, Co, and O tri-doped GCN possess unique electronic structures and high surface areas.

Table 3. The summary of tri-doped GCN.

Dopant	Bandgap Energy (eV)	Precursor/ Synthesis Method	Reaction Condition	Application	Performance of Activity	Ref. (Year)
S, Co, O	2.52	Thiourea, cobalt nitrate hexahydrate, DCDA/Thermal polymerization 520 °C, Hydrothermal 150 °C	250 W high-pressure Na lamp (λ = 400–800)	RhB photodegradation	Rate: 0.0026 min^{-1} 95%, 120 min	[134] (2015)
P, S, O	2.34	Ammonium phosphate, thiourea/Thermal polymerization 550 °C	300 W Xe lamp ($\lambda \geq$ 420 nm)	Water splitting	H_2: 7330 µmol g^{-1}, 3 h	[132] (2019)
P, S, O	2.6–2.7	HCCP, H_2O_2, melamine, sulfur/Thermal polymerization 550 °C	350 W Xe lamp	Methylene blue photodegradation	95%, 2 h	[133] (2020)
Fe, Co, O	N/A	Urea, iron (iii) nitrate nanohydrate, cobalt nitrate hexahydrate/Thermal polymerization 550 °C	N/A	Tetracycline degradation by persulfate activation	90%, 120 min	[135] (2022)

Remark: N/A: Not available; HCCP: Hexachlorotriphosphazene; RhB: Rhodamine B; DCDA: Dicyandiamide.

2.4. Rare-Earth Doping

The doping of rare-earth elements to a GCN structure can be an effective method to promote better photocatalytic reactions. Unlike transition elements that have several different oxidation states, all the elements in the lanthanide series exhibited a +3 oxidation state. It was reported that rare-earth-doped GCN can concentrate the target pollutant on the photocatalyst surface and fasten the photodegradation rate [136]. That may be due to an unfilled 4f orbital that can facilitate photo-induced carrier distribution by acting as a capturing state to suppress photogenerated charge recombination. Table 4 lists the rare-earth-doped GCN reported by researchers. Jin et al. reported on Ce-GCN by thermal polymerization synthesis. Similarly to metal-doped GCN, the metal dopant is coordinated at the center of GCN. That is because the ionic radius of Ce^{3+} was 103 pm, which is much large than C (70 pm) and N (65 pm) atoms, and therefore, substitutional doping is not favorable. Meanwhile, 0.5% doping of Ce-GCN showed 2.12 times better performance in RhB photodegradation compared to bulk GCN (0.0073 min^{-1}), which was 0.0155 min^{-1}. This is mainly because the bandgap energy is reduced from 2.70 to 2.57 eV, and the Ce doping site can trap the photo-excited electrons to prevent charge recombination. It was known that lanthanide ions can act as a Lewis acid in the GCN structure by capturing photo-excited electrons at CB. It was noticed that the doping of Ce to GCN can cause both C1s and N1s peaks, which shifted the binding energy to a higher level. Since Ce is forming a bond with N atoms, the lone pair of electrons from N are transferred to Ce. Thus, the shifting of the binding energy of N1s is mainly because the doping of Ce decreased the electron densities of the N atom in the GCN structure [137]. Yet, due to the high electronegativity of N, the electrons in the C-N bond are closer to the N atom. Therefore, the electron density of C was also affected after introducing Ce dopant to the GCN structure, leading to C1s binding energy shifting. Kulia et al. synthesized Ce-GCN by the chemical-controlled ion-adsorption method; this preparation method can be controlled by several parameters, such as temperature, pH, and the amount of GCN. It was found that the optimum condition for Ce^{3+} ion-adsorption was 25 °C, pH 6, and 0.2 g L^{-1} of GCN. A similar finding to Jin et al., the XPS peak shifting of N1s was detected in the Ce-

GCN structure. Furthermore, the author reported on Atomic Dipole Corrected Hirshfeld (ADCH) charges of several nitrogen atoms; it was found that N from Ce-GCN shows less negative than bulk GCN, confirming that the part of the electron from N has moved to Ce^{3+} (Figure 22). A computational study found that the LUMO–HUMO gap of GCN was increased from 3.48 eV (bulk GCN) to 3.92 eV (Ce-GCN); the large LUMO–HUMO indicates that the Ce-GCN shows higher chemical stability compared to bulk GCN. The Ce from Ce-GCN contributed a high composition to LUMO (α-LUMO: 20.17%, β-LUMO: 5.44%) instead of HOMO (α-SOMO: 0.70%, β-SOMO: 0.73%), revealing that the Ce^{3+} acts as an electron acceptor in GCN structure, that can capture photo-excited electrons to prevent charge recombination. The photodegradation rate of methylene blue was improved from 0.0100 (bulk) to 0.0174 min^{-1} (Ce-GCN) under sunlight irradiation. This is due to the extended light absorption of Ce-GCN at 600–800 nm, retarded charge recombination, and large surface area (86.37 m^2/g) [138].

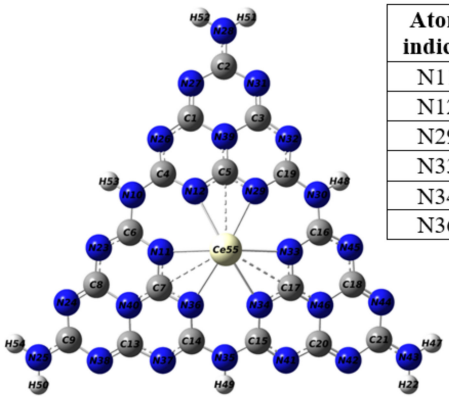

Atom indices	ADCH charge		$(\Delta q)_{Hirshfeld}$
	Isolated g-C_3N_4	g-C_3N_4/Ce^{3+}	
N11	-0.377	-0.351	1.949
N12	-0.377	-0.351	1.949
N29	-0.422	-0.351	1.949
N33	-0.460	-0.351	1.949
N34	-0.460	-0.351	1.949
N36	-0.422	-0.351	1.949

Figure 22. The ADCH charges and charge differences of the nearest carbon and nitrogen atoms adjacent to the central Ce^{3+} ion within Ce-GCN. Reproduced with permission from Ref. [138].

Li et al. reported on Er-GCN with different doping dosages. It was found that excessive Er doping can occupy the active sites of GCN on the surface, which can lower photoactivity. The Er^{3+} can be reduced by trapping an electron (Equation (1)); the electron can then react with oxygen on the GCN surface to form a superoxide anion, and the Er^{2+} is oxidized back to Er^{3+} (Equation (2)). However, excessive Er doping can cause the Er^{3+}/Er^{2+} reduction more rapidly than Er^{2+}/Er^{3+} oxidization, resulting in excess Er ions acting as a recombination center for photogenerated charge carriers. The optimum Er dosage in this study was 0.0070 g of $Er(NO_3)_3 \cdot 5H_2O$ in 2 g of melamine, with 0.0204 min^{-1} of TC removal rate, which was 1.74 times faster than bulk GCN (0.0117 min^{-1}). Apart from that, the author mentioned that the optimum TC photodegradation was in pH 4. That is because the pKa of TC is 3.30, 7.68, and 9.68. When the pH was below 3.30, both TC and Er-GCN were in positive charge, and it is vice versa for pH 7.68 and above. The same charges of both target pollutant and photocatalyst can cause electrostatic repulsion, which is unfavorable for photodegradation. To prevent charge repulsion, the best condition for TC photodegradation was pH 3.30–7.68. In addition, the author reported that an acidic condition is more favorable for the reaction of the photogenerated hole, and therefore, pH 4 was the optimum condition for TC photodegradation. The photocatalyst toxicity test was completed with an *E. coli* test; it was found that the inhibition percentages of all GCNs in the study were 3.25% and lower, indicating that the toxicity was negligible [136].

$$Er^{3+} + e^- \rightarrow Er^{2+} \quad (1)$$

$$Er^{2+} + O_2 \rightarrow Er^{3+} + O_2^{-\bullet} \quad (2)$$

Furthermore, Li et al. also reported on Sm-GCN and mentioned that superoxide anion is the dominant active species for tylosin photodegradation. It was reported that

the optimum pH for photodegradation was pH 7 because the pKa of tylosin is pH 7.1. Excessive protons in the aqueous solution have occurred when the pH is low. The excess protons can react with superoxide anions to form H_2O_2, which reduces the number of active species in the reaction. Meanwhile, a high pH value can cause an excess of OH^- in the aqueous solution; the OH^- can react with photogenerated holes to produce water and lower the photodegradation rate. Foreign anions such as nitrate, sulfate, and chloride can interfere with the photodegradation performance of tylosin. That is because these anions can consume the active species in an aqueous system to oxidize themselves [139]. Nonetheless, Sm-GCN (0.0165 min^{-1}) has a better tylosin photodegradation rate than Er-GCN (0.0131 min^{-1}) in 90 min, indicating that Sm-GCN was more efficient in photocatalysis. Sarkar et al. reported a DFT study in which higher atomic numbers of lanthanides such as Gd, Eu, and Sm have better photocatalytic performance due to better photo-electron transfer, high electrophilicity, and stronger HOMO–LUMO delocalization compared to low atomic numbers of lanthanides [140].

Wang et al. synthesized Eu-GCN by adding diluted nitric acid to melamine and Eu_2O_3 with thermal polymerization. The purpose of adding diluted nitric acid is to form melaminium cation by protonating the melamine. The melaminium cation will then exhibit a layered structure by connecting nitrate anions. The nitrate anions will then produce huge amounts of gases during thermal calcination, leaving nanosheets with a high surface area. The introduction of Eu^{3+} has caused the nanosheets to form a hollow morphology, which may be due to Eu^{3+} connecting with C-N and producing a lantern-like morphology (Figure 23). The lantern-like hollow structure of Eu-GCN has brought a few advantages, which are (i) high surface area, (ii) the inner surface of the hollow structure promoting light scattering and reflection, which improves the light utilization, and (iii) shortening the charge diffusion distance. This finding was similar to another research group that studied Tb-GCN for tylosin photodegradation [141]. The surface area of Eu-GCN was 137.2 m^2/g, which is 6.5 times higher than bulk GCN (21.1 m^2/g). The light absorption edge was enhanced from 445 to 493 nm due to the introduction of the Eu^{3+} impurity state. As a result, the TC photodegradation performance of Eu-GCN (0.03330 min^{-1}) was 1.71 times stronger than bulk GCN (0.01945 min^{-1}) [142]. Tang et al. reported on Eu-GCN for CO_2 reduction and water-splitting applications. The Eu-GCN was prepared by two-step calcination synthesis, which is (i) thermal calcination of urea for 550 °C and (ii) $Eu(NO_3)_3{\cdot}6H_2O$ was added to GCN and further calcined at 380 °C. The surface area of Eu-GCN was improved from 57.9 (bulk GCN) to 111.3 m^2/g, which was 1.92 times better than bulk. The H_2 production was 78.1 μmol h^{-1} g^{-1}, which is 7.3 times better than bulk GCN (10.7 μmol g^{-1} h^{-1}) [143]. Tang et al. reported on Eu-GCN in the same year, but the synthesis method was slightly different. The Eu-GCN was prepared by one-pot synthesis for this time, which was mixing $Eu(NO_3)_3{\cdot}6H_2O$ and urea for 550 °C calcination, and the final Eu-GCN is formed. The highest surface area of Eu-GCN in this study was 90.1 m^2/g, which was slightly lower than the previous study (111.3 m^2/g). One of the reasons that can explain the higher surface area in the previous study was due to the two-step calcination process. It was reported that double calcination can enlarge the surface area, but the light absorption will slightly drop [3]. As a result, the bandgap of Eu-GCN in the previous study was 2.60 eV, which was broader than Eu-GCN in this study (2.55 eV) [144]. This reveals that the synthesis method and conditions can alter the GCN properties.

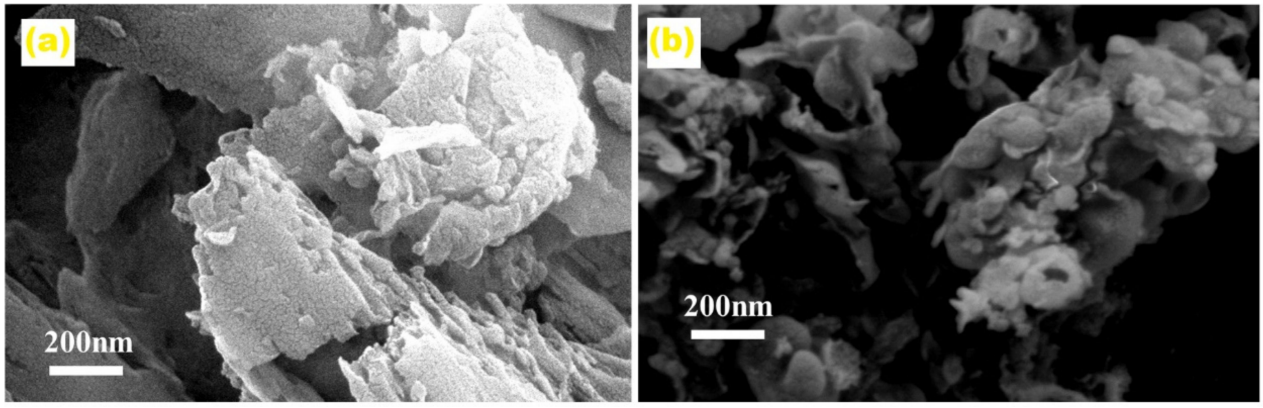

Figure 23. The FESEM image of (**a**) bulk GCN shows a flat surface, and (**b**) Eu-GCN shows a lantern-like hollow surface. Reproduced with permission from Ref. [142].

A few works of literature reported on multi-element-doped rare-earth GCN. As mentioned above, most of the lanthanides in GCN functioned as electron trapping to prolong the charge carrier lifetime. Guo et al. prepared B, Eu-GCN for TC photodegradation. The function of the B dopant can create an impurity state above VB to promote lower energy for charge excitation. As a result, B, Eu-GCN has four possible pathways for charge activation, which are (i) photo-excited electron transfer from VB to CB, (ii) photo-excited electron captured by impurity state from Eu^{3+}, (iii) photo-excited electron migrated from B1s impurity state to GCN CB, and (iv) photo-excited electron from B1s is captured by an impurity state of Eu^{3+}. Compared with bulk GCN, the PL intensity of B, Eu-GCN was greatly reduced, indicating that the charge separation efficiency was greatly enhanced due to impurity states. The bandgap energy was reduced from 2.92 (bulk GCN) to 2.83 eV (B, Eu-GCN), because the impurity states slightly lowered the excitation energy. Thus, the TC photodegradation performance was improved from 0.0112 min^{-1} (bulk) to 0.0477 min^{-1} (B, Eu-GCN) in 50 min reaction time. It was found that the VB of B, Eu-GCN was only +1.58 eV (vs. NHE) in this study, which is not positive enough for $OH^-/OH^\bullet$ (+1.99 eV) and $H_2O/OH^\bullet$ (+2.40 eV) reactions to produce $OH^\bullet$. A scavenging test showed that superoxide anion was the dominant active species, which was followed by $OH^\bullet$. Since $OH^\bullet$ is unable to be oxidized by neither water nor OH^-, thus, it was predicted that the $OH^\bullet$ is formed by the reduction in superoxide as in Equations (3) and (4). [145].

$$O_2^{-\bullet} + e^- + 2H^+ \rightarrow H_2O_2 \quad (3)$$

$$H_2O_2 + e^- \rightarrow OH^\bullet + OH^- \quad (4)$$

Wu et al. reported on C, Ce-GCN, by mixing benzoic acid with melamine and $Ce(NO_3)_3 \cdot 6H_2O$ for thermal calcination. The functional group of benzoic acid, COOH, can be easily deprotonated and form a hydrogen bond with melamine. So, it can easily dope the C atom to the GCN structure under thermal calcination. The function of the C dopant is slightly different from the B dopant as mentioned above. C self-doped to the GCN structure can promote better delocalization in between conjugated bonds, which can enhance the electrical conductivity of GCN and provide new channels for the charge carriers' migration. It was reported that the C, Ce-GCN powder shows a darker color compared to bulk GCN, and the light absorption was red-shifted from 470 (bulk GCN) to 530 nm (C, Ce-GCN) based on UV-DRS analysis. The electron delocalization of bulk GCN usually moves in X and Y directions. However, the red-shift is mainly attributed to electron migration along the Z direction [146], meaning that the electron moves toward the Z direction in C, Ce-GCN as well. As a result, the C in GCN promotes extra pathways for electron migration, and the Ce traps these electrons to prevent fast recombination. The average lifetime of charge carriers was 5.84 ns for C, Ce-GCN, which was 1.91 times longer lifetime than bulk GCN (3.05 ns). This study removed 90.1% of TC in an hour, with the photodegradation rate of

0.04027 min^{-1}, which was 5.7 times faster than bulk GCN (0.00706 min^{-1}) [147]. Apart from the use of benzoic acid as the source of carbon dopant, Zhu et al. prepared C, Ce-GCN by using alternanthera philoxeroides griseb (alligator weed) as the source of carbon dopant. The use of alligator weed in this study is due to its high absorption to Ce^{3+}/Ce^{4+}, fast growth, and wide abundance. The alligator weed was initially kept in the Ce salt solution for 2 weeks; then, it was ground into powder and mixed with different amounts of melamine for calcination. This method has successfully synthesized a high crystalline and large surface area (63.8 m^2/g) of C, Ce-GCN. The 2-mercaptobenzothiazole removal was 96.5% in 90 min, which was much better than the bulk GCN (39.0%, 90 min) [148]. This is an alternative way to reduce the production cost and promote green method preparation for C-based-doped GCN, which can relieve environmental pollution.

In addition to non-metal/rare-earth co-doped GCN, Pan et al. reported on metal/rare-earth co-doped GCN by using Fe and Ce cations. It was found that the Fe and Ce cation can undergo a redox reaction (Equation (5)). The Fe^{3+} in the GCN structure can trap the photo-excited electrons by reducing itself to Fe^{2+}. Then, these trapped electrons are transferred to Ce for further trapping, and the Fe^{2+} oxidizes itself back to the Fe^{3+} oxidation state. These electrons will then allow migration to the GCN surface for further reaction. The Fe, Ce-GCN in this study has reduced the bandgap of GCN from 2.65 to 2.53 eV, which is due to the impurity bands extending the visible-light photoactivity. Therefore, the photo-reduction of Cr(VI) was 0.0197 min^{-1}, which was four times better than bulk GCN (0.0049 min^{-1}) [149].

$$Ce^{3+} + Fe^{3+} \rightarrow Ce^{4+} + Fe^{2+} \quad (5)$$

Rare-earth doped GCN does help reduce the photogenerated charge carrier recombination, since the unfilled 4f orbital can temporarily capture the photo-excited electrons. The introduction of rare-earth dopants also creates an impurity state in the GCN band structure, which provide two pathways for electron excitation, which are (i) VB to CB and (ii) VB to impurity state. The VB to impurity state provides lower excitation energy, which causes the light absorption of GCN to be bathochromically shifted to enhance the photoactivity in visible light. Compared to single-doped, multi-element-doped rare-earth GCN would provide an extra impurity state in the GCN band structure and thus perform photocatalysis more effectively. Biomass synthesized GCN will be a great idea to reduce production cost and relieve pollution from the environment. There are still some lanthanides that are not studied for GCN doping, such as Pr, Nd, Pm, and so on.

Table 4. The summary of rare-earth single-doped and co-doped GCN.

Dopant	Bandgap Energy (eV)	Precursor/ Synthesis Method	Light Source for Reaction	Application	Performance of Activity	Ref. (Year)
Ce	2.57	Cerium (IV) sulfate tetrahydrate, melamine/Thermal polymerization 550 °C	250 W high-pressure Na lamp (λ = 400–800 nm)	RhB photodegradation	Rate: 0.0155 min^{-1}	[137] (2015)
Ce	2.70	Urea, cerium nitrate hexahyrate/Chemical controlled ion-adsorption	Sunlight intensity ~ 212 K lux	MB photodegradation	Rate: 0.0174 min^{-1} (95%, 180 min)	[138] (2020)
Er	2.50	Erbium (iii) nitrate pentahydrate, melamine/Thermal polymerization 550 °C	35 W Xe lamp	TC photodegradation	Rate: 0.0204 min^{-1}, 90 min	[136] (2020)
				Tylosin photodegradation	Rate: 0.0131 min^{-1}, 90 min	
				RhB photodegradation	Rate: 0.0747 min^{-1}, 30 min	
Eu	2.48	Nitric acid, melamine, europium (iii) oxide/Thermal polymerization 500 °C	300 W Xe lamp (λ ≥ 420 nm)	RhB photodegradation	Rate: 0.1185 min^{-1} (98%, 50 min)	[142] (2018)
				TC photodegradation	Rate: 0.0333 min^{-1} (82%, 50 min)	
Eu	2.55	Urea, europium nitrate hexahydrate/Thermal polymerization 550 °C	300 W Xe lamp	Water splitting	H_2: 2425.7 μmol g^{-1}, 6 h	[144] (2019)

Table 4. *Cont.*

Dopant	Bandgap Energy (eV)	Precursor/ Synthesis Method	Light Source for Reaction	Application	Performance of Activity	Ref. (Year)
Eu	2.60	Urea, europium nitrate hexahydrate/Thermal polymerization 550 °C, 380 °C	300 W Xe lamp	CO_2 reduction	CH_4: 22.8 μmol h^{-1} g^{-1}	[143] (2019)
				Water splitting	H_2: 78.1 μmol h^{-1} g^{-1}	
Tb	2.47	Terbium(III) nitrate pentahydrate, nitric acid, melamine/Thermal polymerization 550 °C	170 W Xe lamp	TC photodegradation	Rate: 0.0241 min^{-1}	[141] (2021)
				Tylosin photodegradation	Rate: 0.0271 min^{-1}	
Sm	2.5	Samarium (iii) nitrate pentahydrate, nitric acid, melamine/Thermal polymerization 550 °C	35 W Xe lamp	RhB photodegradation	Rate: 0.0727 min^{-1}, 30 min	[139] (2020)
				Tylosin photodegradation	Rate: 0.0165 min^{-1}, 90 min	
Fe, Ce	2.53	Iron (iii) nitrate, cerium nitrate, urea/Thermal polymerization 550 °C, hydrothermal 160 °C	300 W Xe lamp (λ ≥ 420 nm)	Cr(VI) photodegradation	Rate: 0.0197 min^{-1} (99.8%, 120 min)	[149] (2020)
				RhB photodegradation	88.7%, 120 min	
C, Ce	2.55	Melamine, benzoic acid, cerium nitrate hexahydrate/Thermal polymerization 550 °C	300 W Xe lamp (λ ≥ 420 nm)	TC photodegradation	90.1%, 60 min	[147] (2020)
				RhB photodegradation	99.4%, 120 min	
C, Ce	2.70	Ce salt, alternanthera philoxeriodes griseb, melamine/Thermal polymerization 500 °C	300 W Xe lamp (λ ≥ 420 nm)	2-MBT photodegradation	96.5%, 90 min	[148] (2020)
B, Eu	2.81	Nitric acid, melamine, europium (iii) oxide, boric acid/Thermal polymerization 550 °C	400 W halogen lamp	TC photodegradation	Rate: 0.0477 min^{-1} (90.8%, 50 min)	[145] (2021)
B, Eu (composite with MoS_2)	2.88	Nitric acid, melamine, europium (iii) oxide, boric acid/Thermal polymerization 550 °C Ammonium molybdate tetrahydrate, thiourea/Hydrothermal 200 °C	400 W halogen lamp	TC photodegradation	Rate: 0.0873 min^{-1} (99.0%, 50 min)	[150] (2021)
Mn, Ce	N/A	Cerium (iii) chloride heptahydrate, manganese chloride tetrahydrate, urea, formic acid/Thermal polymerization 520 °C	N/A	2,4-DCP Degradation	Rate: 0.156 min^{-1} (100%, 30 min)	[151] (2022)
Gd, Ce, Sm, Er	2.19	Melamine, cerium chloride pentahydrate, erbium nitrate pentahydrate, samarium nitrate hexahydrate, gadolinium nitrate hexahydrate/Thermal polymerization 550 °C	300 W Xe lamp (λ ≥ 420 nm)	Naproxen photodegradation	Rate: 0.0085 min^{-1} (82.0%, 180 min)	[152] (2022)

Remark: N/A: Not available; 2-MBT: 2-mercaptobenzothiazole; TC: Tetracycline; RhB: Rhodamine B; MB: Methylene blue; 2,4-DCP: 2,4-dichlorophenol.

3. Conclusions and Prospects

Pristine GCN consists of several limitations, such as fast recombination, limited light absorption, and small surface area. These limitations require to be solved to enhance photoactivity. Each elemental doping can play a different function in GCN. For example, metal and rare-earth-doped GCN can provide a defect state for photo-excited trapping and thus prolong the charge carrier's lifetime. Non-metal doped GCN usually alters the VBM or CBM of band structures to provide extra electrons for photocatalysis. C-based GCN provides fast electron delocalization in X, Y, and Z-axis pathways to allow more electrons to migrate on the GCN surface for photoreaction. O-based GCN usually can increase the hydrophilicity of GCN and enhance the surface contact in aqueous reactions. Molten-state synthesis can produce high crystallinity of GCN, which is beneficial for electron migration with GCN structures. However, some dopants can inhibit the crystal growth of GCN, leading to low crystallinity. The low crystallinity is due to the drastic decomposition of GCN during thermal calcination, producing a high surface area of GCN, which is also good for photoactivity. In addition, the low surface area of GCN can be improved by a few methods, such as (i) introducing a template, (ii) recalcination, (iii) addition of nitric acid, and (iv) freeze drying. It was found that recalcination and the addition of nitric acid are the simpler, safer, and more economical ways to produce ultrathin GCN nanosheets. Nonetheless, introducing a template can produce a uniform pore size distribution of GCN. Meanwhile, the hollow structure of GCN can cause light scattering and reflection

and improve light utilization. To date, some of the elements are still not yet studied by researchers, such as Br, Li, Mg, Si, Nb, Pr, Pm-based co-doped, and tri-doping. Instead of single doping, multi-element doped GCN is important in photocatalytic application study because it can solve several issues with one solution, such as extending the light absorption by tuning the bandgap, suppressing the charge recombination, and enhancing the surface morphology. It was suggested that p-n junction GCN can be produced by co-doping of a p-type element and an n-type element. The p-n junction can form an electrical potential that allows electrons and holes to transfer to the opposite direction and facilitate a better photocatalytic reaction. In order to make sure the photocatalysts are stable, safe, and have no leaching during photocatalysis, it is encouraged to perform a toxicity assessment for the photocatalyst and compare the structure of the photocatalyst before and after photoreaction to make sure the photocatalyst is stable.

Author Contributions: Conceptualization and supervision: G.-T.P. and B.F.L.; writing—original draft preparation: B.L.P., C.C.O. and K.-C.L.; review and editing, artwork and schemes: B.F.L., B.L.P., S.C. and K.-L.P. All authors have read and agreed to the published version of the manuscript.

Funding: This work is supported by Universiti Malaya, Institute of Research and Management (Grant number: Student Financial Aid 2019) and Ministry of Science and Technology of Taiwan, the Republic of China (Grant number: MOST 110-2637-E-027-007-).

Data Availability Statement: Not applicable.

Conflicts of Interest: The authors declare no conflict of interest.

References

1. Center, B.P. *Annual Energy Outlook 2020*; Energy Information Administration: Washington, DC, USA, 2020; Volume 12, pp. 1672–1679.
2. Vohra, K.; Vodonos, A.; Schwartz, J.; Marais, E.A.; Sulprizio, M.P.; Mickley, L.J. Global mortality from outdoor fine particle pollution generated by fossil fuel combustion: Results from GEOS-Chem. *Environ. Res.* **2021**, *195*, 110754. [CrossRef] [PubMed]
3. Phoon, B.L.; Lai, C.W.; Pan, G.-T.; Yang, T.C.-K.; Juan, J.C. Highly mesoporous g-C_3N_4 with uniform pore size distribution via the template-free method to enhanced solar-driven tetracycline degradation. *Nanomaterials* **2021**, *11*, 2041. [CrossRef] [PubMed]
4. Phoon, B.L.; Ong, C.C.; Saheed, M.S.M.; Show, P.-L.; Chang, J.-S.; Ling, T.C.; Lam, S.S.; Juan, J.C. Conventional and emerging technologies for removal of antibiotics from wastewater. *J. Hazard. Mater.* **2020**, *400*, 122961. [CrossRef] [PubMed]
5. Mohd Yatim, A.A.; Ismail, N.A.; Hamid, M.R.Y.; Mohd Adnan, M.A.; Phoon, B.L.; Johan, M.R.; Lee, K.M. Vanadium and nitrogen co-doped titanium dioxide (TiO_2) with enhanced photocatalytic performance: Potential in wastewater treatment. *J. Nanosci. Nanotechnol.* **2020**, *20*, 741–751. [CrossRef]
6. UshaVipinachandran, V.; Rajendran, S.; Badagoppam Haroon, K.H.; Ashokan, I.; Mondal, A.; Bhunia, S.K. Detoxification of endocrine disruptors in water using visible-light-active nanostructures: A review. *ACS Appl. Nano Mater.* **2020**, *3*, 11659–11687. [CrossRef]
7. Dong, L.; Hou, L.A.; Wang, Z.; Gu, P.; Chen, G.; Jiang, R. A new function of spent activated carbon in BAC process: Removing heavy metals by ion exchange mechanism. *J. Hazard. Mater.* **2018**, *359*, 76–84. [CrossRef]
8. Zhu, X.; Li, B.; Yang, J.; Li, Y.; Zhao, W.; Shi, J.; Gu, J. Effective adsorption and enhanced removal of organophosphorus pesticides from aqueous solution by Zr-based MOFs of UiO-67. *ACS Appl. Mater. Interfaces* **2015**, *7*, 223–231. [CrossRef]
9. Oliveira, J.T.; de Sousa, M.C.; Martins, I.A.; de Sena, L.M.G.; Nogueira, T.R.; Vidal, C.B.; Neto, E.F.A.; Romero, F.B.; Campos, O.S.; do Nascimento, R.F. Electrocoagulation/oxidation/flotation by direct pulsed current applied to the removal of antibiotics from Brazilian WWTP effluents. *Electrochim. Acta* **2021**, *388*, 138499. [CrossRef]
10. Kim, S.D.; Cho, J.; Kim, I.S.; Vanderford, B.J.; Snyder, S.A. Occurrence and removal of pharmaceuticals and endocrine disruptors in South Korean surface, drinking, and waste waters. *Water Res.* **2007**, *41*, 1013–1021. [CrossRef]
11. Kümmerer, K. Antibiotics in the aquatic environment—A review—Part II. *Chemosphere* **2009**, *75*, 435–441. [CrossRef]
12. De Toni, L.; Tisato, F.; Seraglia, R.; Roverso, M.; Gandin, V.; Marzano, C.; Padrini, R.; Foresta, C. Phthalates and heavy metals as endocrine disruptors in food: A study on pre-packed coffee products. *Toxicol. Rep.* **2017**, *4*, 234–239. [CrossRef]
13. Ghanbarlou, H.; Pedersen, N.L.; Nikbakht Fini, M.; Muff, J. Synergy optimization for the removal of dye and pesticides from drinking water using granular activated carbon particles in a 3D electrochemical reactor. *Environ. Sci. Pollut. Res.* **2020**, *27*, 22206–22213. [CrossRef]
14. Phoon, B.L.; Pan, G.-T.; Yang, T.C.-K.; Lee, K.M.; Lai, C.W.; Juan, J.C. Facile preparation of nanocrystalline TiO_2 thin films using electrophoretic deposition for enhancing photoelectrochemical water splitting response. *J. Mater. Sci. Mater. Electron.* **2017**, *28*, 16244–16253. [CrossRef]

15. Sanakousar, F.; Vidyasagar, C.; Jiménez-Pérez, V.; Prakash, K. Recent progress on visible-light-driven metal and non-metal doped ZnO nanostructures for photocatalytic degradation of organic pollutants. *Mater. Sci. Semicond. Process.* **2022**, *140*, 106390. [CrossRef]
16. Phoon, B.L.; Lai, C.W.; Pan, G.-T.; Yang, T.C.-K.; Juan, J.C. One-pot hydrothermal synthesis of strontium titanate nanoparticles photoelectrode using electrophoretic deposition for enhancing photoelectrochemical water splitting. *Ceram. Int.* **2018**, *44*, 9923–9933. [CrossRef]
17. Phoon, B.L.; Lai, C.W.; Juan, J.C.; Show, P.-L.; Pan, G.-T. Recent developments of strontium titanate for photocatalytic water splitting application. *Int. J. Hydrogen Energy* **2019**, *44*, 14316–14340. [CrossRef]
18. Qian, X.; Meng, X.; Sun, J.; Jiang, L.; Wang, Y.; Zhang, J.; Hu, X.; Shalom, M.; Zhu, J. Salt-assisted synthesis of 3D porous g-C_3N_4 as a bifunctional photo-and electrocatalyst. *ACS Appl. Mater. Interfaces* **2019**, *11*, 27226–27232. [CrossRef]
19. Xu, Q.; Cheng, B.; Yu, J.; Liu, G. Making co-condensed amorphous carbon/g-C_3N_4 composites with improved visible-light photocatalytic H_2-production performance using Pt as cocatalyst. *Carbon* **2017**, *118*, 241–249. [CrossRef]
20. Rameshbabu, R.; Ravi, P.; Sathish, M. Cauliflower-like CuS/ZnS nanocomposites decorated g-C_3N_4 nanosheets as noble metal-free photocatalyst for superior photocatalytic water splitting. *Chem. Eng. J.* **2019**, *360*, 1277–1286. [CrossRef]
21. Cui, Y.; Zhang, J.; Zhang, G.; Huang, J.; Liu, P.; Antonietti, M.; Wang, X. Synthesis of bulk and nanoporous carbon nitride polymers from ammonium thiocyanate for photocatalytic hydrogen evolution. *J. Mater. Chem.* **2011**, *21*, 13032–13039. [CrossRef]
22. Ke, P.; Zeng, D.; Cui, J.; Li, X.; Chen, Y. Improvement in Structure and Visible Light Catalytic Performance of g-C_3N_4 Fabricated at a Higher Temperature. *Catalysts* **2022**, *12*, 247. [CrossRef]
23. Patnaik, S.; Sahoo, D.P.; Parida, K. Recent advances in anion doped g-C_3N_4 photocatalysts: A review. *Carbon* **2021**, *172*, 682–711. [CrossRef]
24. Zhao, G.-Q.; Zou, J.; Hu, J.; Long, X.; Jiao, F.-P. A critical review on graphitic carbon nitride (g-C_3N_4)-based composites for environmental remediation. *Sep. Purif. Technol.* **2021**, *279*, 119769. [CrossRef]
25. Liu, X.; Ma, R.; Zhuang, L.; Hu, B.; Chen, J.; Liu, X.; Wang, X. Recent developments of doped g-C_3N_4 photocatalysts for the degradation of organic pollutants. *Crit. Rev. Environ. Sci. Technol.* **2021**, *51*, 751–790. [CrossRef]
26. Ma, H.; Li, Y.; Li, S.; Liu, N. Novel PO codoped g-C_3N_4 with large specific surface area: Hydrothermal synthesis assisted by dissolution–precipitation process and their visible light activity under anoxic conditions. *Appl. Surf. Sci.* **2015**, *357*, 131–138. [CrossRef]
27. Wang, X.; Maeda, K.; Thomas, A.; Takanabe, K.; Xin, G.; Carlsson, J.M.; Domen, K.; Antonietti, M. A metal-free polymeric photocatalyst for hydrogen production from water under visible light. *Nat. Mater.* **2009**, *8*, 76–80. [CrossRef]
28. He, Y.; Cai, J.; Zhang, L.; Wang, X.; Lin, H.; Teng, B.; Zhao, L.; Weng, W.; Wan, H.; Fan, M. Comparing two new composite photocatalysts, t-$LaVO_4$/g-C_3N_4 and m-$LaVO_4$/g-C_3N_4, for their structures and performances. *Ind. Eng. Chem. Res.* **2014**, *53*, 5905–5915. [CrossRef]
29. Holst, J.R.; Gillan, E.G. From triazines to heptazines: Deciphering the local structure of amorphous nitrogen-rich carbon nitride materials. *J. Am. Chem. Soc.* **2008**, *130*, 7373–7379. [CrossRef]
30. Xu, Y.; Gao, S.-P. Band gap of C_3N_4 in the GW approximation. *Int. J. Hydrogen Energy* **2012**, *37*, 11072–11080. [CrossRef]
31. Appaturi, J.N.; Ratti, R.; Phoon, B.L.; Batagarawa, S.M.; Din, I.U.; Selvaraj, M.; Ramalingam, R.J. A review of the recent progress on heterogeneous catalysts for Knoevenagel condensation. *Dalton Trans.* **2021**, *50*, 4445–4469. [CrossRef]
32. Sattler, A.; Pagano, S.; Zeuner, M.; Zurawski, A.; Gunzelmann, D.; Senker, J.; Müller-Buschbaum, K.; Schnick, W. Melamine–melem adduct phases: Investigating the thermal condensation of melamine. *Chem. Eur. J.* **2009**, *15*, 13161–13170. [CrossRef] [PubMed]
33. Zhu, J.; Wei, Y.; Chen, W.; Zhao, Z.; Thomas, A. Graphitic carbon nitride as a metal-free catalyst for NO decomposition. *Chem. Commun.* **2010**, *46*, 6965–6967. [CrossRef] [PubMed]
34. Wen, J.; Xie, J.; Chen, X.; Li, X. A review on g-C_3N_4-based photocatalysts. *Appl. Surf. Sci.* **2017**, *391*, 72–123. [CrossRef]
35. Zhang, J.; Ma, Z. Porous g-C_3N_4 with enhanced adsorption and visible-light photocatalytic performance for removing aqueous dyes and tetracycline hydrochloride. *Chin. J. Chem. Eng.* **2018**, *26*, 753–760. [CrossRef]
36. Pawar, R.C.; Kang, S.; Han, H.; Choi, H.; Lee, C.S. In situ reduction and exfoliation of g-C_3N_4 nanosheets with copious active sites via a thermal approach for effective water splitting. *Catal. Sci. Technol.* **2019**, *9*, 1004–1012. [CrossRef]
37. Papailias, I.; Todorova, N.; Giannakopoulou, T.; Ioannidis, N.; Boukos, N.; Athanasekou, C.P.; Dimotikali, D.; Trapalis, C. Chemical vs thermal exfoliation of g-C_3N_4 for NOx removal under visible light irradiation. *Appl. Catal. B Environ.* **2018**, *239*, 16–26. [CrossRef]
38. Chen, J.; Xiao, X.; Wang, Y.; Ye, Z. Ag nanoparticles decorated WO3/g-C_3N_4 2D/2D heterostructure with enhanced photocatalytic activity for organic pollutants degradation. *Appl. Surf. Sci.* **2019**, *467*, 1000–1010. [CrossRef]
39. Xie, Z.; Feng, Y.; Wang, F.; Chen, D.; Zhang, Q.; Zeng, Y.; Lv, W.; Liu, G. Construction of carbon dots modified MoO3/g-C_3N_4 Z-scheme photocatalyst with enhanced visible-light photocatalytic activity for the degradation of tetracycline. *Appl. Catal. B Environ.* **2018**, *229*, 96–104. [CrossRef]
40. Huang, K.; Hong, Y.; Yan, X.; Huang, C.; Chen, J.; Chen, M.; Shi, W.; Liu, C. Hydrothermal synthesis of g-C_3N_4/$CdWO_4$ nanocomposite and enhanced photocatalytic activity for tetracycline degradation under visible light. *CrystEngComm* **2016**, *18*, 6453–6463. [CrossRef]
41. Scanlon, D.O.; Dunnill, C.W.; Buckeridge, J.; Shevlin, S.A.; Logsdail, A.J.; Woodley, S.M.; Catlow, C.R.A.; Powell, M.J.; Palgrave, R.G.; Parkin, I.P. Band alignment of rutile and anatase TiO_2. *Nat. Mater.* **2013**, *12*, 798–801. [CrossRef]

42. Hou, J.; Yang, C.; Wang, Z.; Zhou, W.; Jiao, S.; Zhu, H. In situ synthesis of α–β phase heterojunction on Bi_2O_3 nanowires with exceptional visible-light photocatalytic performance. *Appl. Catal. B Environ.* **2013**, *142*, 504–511. [CrossRef]
43. Muhmood, T.; Khan, M.A.; Xia, M.; Lei, W.; Wang, F.; Ouyang, Y. Enhanced photo-electrochemical, photo-degradation and charge separation ability of graphitic carbon nitride (g-C_3N_4) by self-type metal free heterojunction formation for antibiotic degradation. *J. Photochem. Photobiol. A Chem.* **2017**, *348*, 118–124. [CrossRef]
44. Que, M.; Cai, W.; Chen, J.; Zhu, L.; Yang, Y. Recent advances in g-C_3N_4 composites within four types of heterojunctions for photocatalytic CO_2 reduction. *Nanoscale* **2021**, *13*, 6692–6712. [CrossRef]
45. Liu, X.; Zhang, Q.; Ma, D. Advances in 2D/2D Z-scheme heterojunctions for photocatalytic applications. *Sol. RRL* **2021**, *5*, 2000397. [CrossRef]
46. Panneri, S.; Ganguly, P.; Mohan, M.; Nair, B.N.; Mohamed, A.A.P.; Warrier, K.G.; Hareesh, U. Photoregenerable, bifunctional granules of carbon-doped g-C_3N_4 as adsorptive photocatalyst for the efficient removal of tetracycline antibiotic. *ACS Sustain. Chem. Eng.* **2017**, *5*, 1610–1618. [CrossRef]
47. Palanivel, B.; Hu, C.; Shkir, M.; AlFaify, S.; Ibrahim, F.A.; Hamdy, M.S.; Mani, A. Fluorine doped g-C_3N_4 coupled $NiFe_2O_4$ heterojunction: Consumption of H_2O_2 for production of hydroxyl radicals towards paracetamol degradation. *Colloid Interface Sci. Commun.* **2021**, *42*, 100410. [CrossRef]
48. Zhang, S.; Gao, L.; Fan, D.; Lv, X.; Li, Y.; Yan, Z. Synthesis of boron-doped g-C_3N_4 with enhanced electro-catalytic activity and stability. *Chem. Phys. Lett.* **2017**, *672*, 26–30. [CrossRef]
49. Starukh, H.; Praus, P. Doping of graphitic carbon nitride with non-metal elements and its applications in photocatalysis. *Catalysts* **2020**, *10*, 1119. [CrossRef]
50. Zhu, Q.-H.; Chen, Z.; Tang, L.-N.; Zhong, Y.; Zhao, X.-F.; Zhang, L.-Z.; Li, J.-H. K and halogen binary-doped graphitic carbon nitride (g-C_3N_4) toward enhanced visible light hydrogen evolution. *Int. J. Hydrogen Energy* **2019**, *44*, 27704–27712. [CrossRef]
51. Jing, J.; Chen, Z.; Feng, C. Dramatically enhanced photoelectrochemical properties and transformed p/n type of g-C_3N_4 caused by K and I co-doping. *Electrochim. Acta* **2019**, *297*, 488–496. [CrossRef]
52. Guo, Y.; Liu, Q.; Li, Z.; Zhang, Z.; Fang, X. Enhanced photocatalytic hydrogen evolution performance of mesoporous graphitic carbon nitride co-doped with potassium and iodine. *Appl. Catal. B Environ.* **2018**, *221*, 362–370. [CrossRef]
53. Li, Y.; Zhang, D.; Feng, X.; Xiang, Q. Enhanced photocatalytic hydrogen production activity of highly crystalline carbon nitride synthesized by hydrochloric acid treatment. *Chin. J. Catal.* **2020**, *41*, 21–30. [CrossRef]
54. Chen, L.; Zhu, D.; Li, J.; Wang, X.; Zhu, J.; Francis, P.S.; Zheng, Y. Sulfur and potassium co-doped graphitic carbon nitride for highly enhanced photocatalytic hydrogen evolution. *Appl. Catal. B Environ.* **2020**, *273*, 119050. [CrossRef]
55. Gorai, D.K.; Kundu, T. Influence of Pt and P doping on the performance of g-C_3N_4 monolayer. *Mater. Manuf. Processes* **2020**, *35*, 625–634. [CrossRef]
56. Ma, Z.; Cui, Z.; Lv, Y.; Sa, R.; Wu, K.; Li, Q. Three-in-One: Opened Charge-transfer channel, positively shifted oxidation potential, and enhanced visible light response of g-C_3N_4 photocatalyst through K and S Co-doping. *Int. J. Hydrogen Energy* **2020**, *45*, 4534–4544. [CrossRef]
57. Ma, X.; Lv, Y.; Xu, J.; Liu, Y.; Zhang, R.; Zhu, Y. A strategy of enhancing the photoactivity of g-C_3N_4 via doping of nonmetal elements: A first-principles study. *J. Phys. Chem. C* **2012**, *116*, 23485–23493. [CrossRef]
58. Li, Y.; Zhu, S.; Liang, Y.; Li, Z.; Wu, S.; Chang, C.; Luo, S.; Cui, Z. One-step synthesis of Mo and S co-doped porous g-C_3N_4 nanosheets for efficient visible-light photocatalytic hydrogen evolution. *Appl. Surf. Sci.* **2021**, *536*, 147743. [CrossRef]
59. Fang, W.; Liu, J.; Yu, L.; Jiang, Z.; Shangguan, W. Novel (Na, O) co-doped g-C_3N_4 with simultaneously enhanced absorption and narrowed bandgap for highly efficient hydrogen evolution. *Appl. Catal. B Environ.* **2017**, *209*, 631–636. [CrossRef]
60. Lu, H.; Li, X.; Li, F.; Xu, X.; Zhao, R.; Xiong, C.; Hu, Q.; Miao, Z.; Tian, M. Construction of single-atom Ag embedded O, K co-doped g-C_3N_4 with enhanced photocatalytic efficiency for tetracycline degradation and Escherichia coli disinfection under visible light. *J. Mol. Liq.* **2022**, *352*, 118655. [CrossRef]
61. She, P.; Yao, C.; Li, J.; Bao, H.; Xu, X.; Zhou, H. One pot synthesis of Ti and O co-doped g-C_3N_4: A novel composite for efficient visible-light-driven photocatalytic inactivation of E. cloacae. *Mater. Res. Express* **2021**, *8*, 125006. [CrossRef]
62. Xu, X.; Wang, S.; Hu, T.; Yu, X.; Wang, J.; Jia, C. Fabrication of Mn/O co-doped g-C_3N_4: Excellent charge separation and transfer for enhancing photocatalytic activity under visible light irradiation. *Dye. Pigment.* **2020**, *175*, 108107. [CrossRef]
63. Wei, H.; Zhang, Y.; Zhang, G.; Cui, J.; Wang, Y.; Qin, Y.; Zhang, X.; Tan, H.H.; Liu, J.; Wu, Y. In situ W/O Co-doped hollow carbon nitride tubular structures with enhanced visible-light-driven photocatalytic performance for hydrogen evolution. *Int. J. Hydrogen Energy* **2021**, *46*, 234–246. [CrossRef]
64. Chi, X.; Liu, F.; Gao, Y.; Song, J.; Guan, R.; Yuan, H. An efficient B/Na co-doped porous g-C_3N_4 nanosheets photocatalyst with enhanced photocatalytic hydrogen evolution and degradation of tetracycline under visible light. *Appl. Surf. Sci.* **2022**, *576*, 151837. [CrossRef]
65. Ruan, Z.-H.; Gao, X.-Y.; Yuan, Y.; Tan, H.-P. Theoretical insight into the effect of Br, Na co-doping on electronic structure, photocatalytic and optical characteristics of g-C_3N_4 using first-principles and optical simulations. *J. Mater. Sci.* **2021**, *56*, 10382–10392. [CrossRef]
66. Roselin, L.S.; Patel, N.; Khayyat, S.A. Codoped g-C_3N_4 nanosheet for degradation of organic pollutants from oily wastewater. *Appl. Surf. Sci.* **2019**, *494*, 952–958. [CrossRef]

67. Wang, J.-C.; Hou, Y.; Feng, F.-D.; Wang, W.-X.; Shi, W.; Zhang, W.; Li, Y.; Lou, H.; Cui, C.-X. A recyclable molten-salt synthesis of B and K co-doped g-C_3N_4 for photocatalysis of overall water vapor splitting. *Appl. Surf. Sci.* **2021**, *537*, 148014. [CrossRef]
68. Hu, S.; Ma, L.; You, J.; Li, F.; Fan, Z.; Lu, G.; Liu, D.; Gui, J. Enhanced visible light photocatalytic performance of g-C_3N_4 photocatalysts co-doped with iron and phosphorus. *Appl. Surf. Sci.* **2014**, *311*, 164–171. [CrossRef]
69. Nguyen, T.-B.; Huang, C.; Doong, R.-A.; Chen, C.-W.; Dong, C.-D. Visible-light photodegradation of sulfamethoxazole (SMX) over Ag-P-codoped g-C_3N_4 (Ag-P@UCN) photocatalyst in water. *Chem. Eng. J.* **2020**, *384*, 123383. [CrossRef]
70. Chen, D.; Liu, J.; Jia, Z.; Fang, J.; Yang, F.; Tang, Y.; Wu, K.; Liu, Z.; Fang, Z. Efficient visible-light-driven hydrogen evolution and Cr (VI) reduction over porous P and Mo co-doped g-C_3N_4 with feeble N vacancies photocatalyst. *J. Hazard. Mater.* **2019**, *361*, 294–304. [CrossRef]
71. Duan, Y.; Li, Y.; Shang, X.; Jia, D.; Li, C. Phosphorus and bismuth co-doped porous g-C_3N_4 nanosheets as an efficient visible-light-driven photocatalyst. *J. Mater. Sci. Mater. Electron.* **2020**, *31*, 1703–1714. [CrossRef]
72. Cao, S.; Huang, Q.; Zhu, B.; Yu, J. Trace-level phosphorus and sodium co-doping of g-C_3N_4 for enhanced photocatalytic H_2 production. *J. Power Sources* **2017**, *351*, 151–159. [CrossRef]
73. Chen, K.-L.; Zhang, S.-S.; Yan, J.-Q.; Peng, W.; Lei, D.-P.; Huang, J.-H. Excellent visible light photocatalytic efficiency of Na and S co-doped g-C_3N_4 nanotubes for H_2 production and organic pollutant degradation. *Int. J. Hydrogen Energy* **2019**, *44*, 31916–31929. [CrossRef]
74. Yang, X.; Cao, C.; Guo, Z.; Zhang, X.; Wang, Y.; Yang, W. Promoting hydrogen evolution of a g-C_3N_4-based photocatalyst by indium and phosphorus co-doping. *New J. Chem.* **2021**, *45*, 7231–7238. [CrossRef]
75. Bahadoran, A.; Najafizadeh, M.; Liu, Q.; De Lile, J.R.; Zhang, D.; Masudy-Panah, S.; Ramakrishna, S.; Fakhri, A.; Gupta, V.K. Co-doping silver and iron on graphitic carbon nitride-carrageenan nanocomposite for the photocatalytic process, rapidly colorimetric detection and antibacterial properties. *Surf. Interfaces* **2021**, *26*, 101279. [CrossRef]
76. Guo, W.; Zhang, J.; Li, G.; Xu, C. Enhanced photocatalytic activity of P-type (K, Fe) co-doped g-C_3N_4 synthesized in self-generated NH3 atmosphere. *Appl. Surf. Sci.* **2019**, *470*, 99–106. [CrossRef]
77. Wu, Y.; Xu, W.; Niandu, W.; Wang, Z.; Wang, Y.; Zhang, Y.; Zhong, W.; Cai, H.-L.; Wu, X. Bridging and bonding: Zinc and potassium co-assisted crystalline g-C_3N_4 for significant highly efficient upon photocatalytic hydrogen evolution. *Appl. Surf. Sci.* **2021**, *542*, 148620. [CrossRef]
78. Lu, Z.-Z.; Li, S.-Q.; Xiao, J.-Y. Synergetic Effect of Na–Ca for Enhanced Photocatalytic Performance in NOX Degradation by g-C_3N_4. *Catal. Lett.* **2021**, *151*, 370–381. [CrossRef]
79. Dong, H.; Zuo, Y.; Song, N.; Hong, S.; Xiao, M.; Zhu, D.; Sun, J.; Chen, G.; Li, C. Bimetallic synergetic regulating effect on electronic structure in cobalt/vanadium co-doped carbon nitride for boosting photocatalytic performance. *Appl. Catal. B Environ.* **2021**, *287*, 119954. [CrossRef]
80. Liu, Z.; Guo, W.; Liu, X.; Wu, G.; Tang, Y.; Mo, Z.; Yang, D. Study on photoelectric properties of Fe-Co codoped g-C_3N_4. *Chem. Phys. Lett.* **2021**, *781*, 138951. [CrossRef]
81. Shen, H.; Li, M.; Guo, W.; Li, G.; Xu, C. P, K co-doped porous g-C_3N_4 with enhanced photocatalytic activity synthesized in vapor and self-producing NH3 atmosphere. *Appl. Surf. Sci.* **2020**, *507*, 145086. [CrossRef]
82. Long, D.; Chen, W.; Zheng, S.; Rao, X.; Zhang, Y. Barium-and phosphorus-codoped g-C_3N_4 microtubes with efficient photocatalytic H_2 evolution under visible light irradiation. *Ind. Eng. Chem. Res.* **2020**, *59*, 4549–4556. [CrossRef]
83. Xu, J.; Chen, Y.; Chen, M.; Wang, J.; Wang, L. In situ growth strategy synthesis of single-atom nickel/sulfur co-doped g-C_3N_4 for efficient photocatalytic tetracycline degradation and CO_2 reduction. *Chem. Eng. J.* **2022**, *442*, 136208. [CrossRef]
84. Ye, J.; Yang, D.; Dai, J.; Li, C.; Yan, Y.; Wang, Y. Strongly coupled cobalt/oxygen co-doped porous g-C_3N_4 heterostructure with abundant oxygen vacancies modulated the peroxymonosulfate activation pathway. *Chem. Eng. J.* **2022**, *431*, 133972. [CrossRef]
85. Guo, Y.; Chen, T.; Liu, Q.; Zhang, Z.; Fang, X. Insight into the enhanced photocatalytic activity of potassium and iodine codoped graphitic carbon nitride photocatalysts. *J. Phys. Chem. C* **2016**, *120*, 25328–25337. [CrossRef]
86. Wang, K.-L.; Li, Y.; Sun, T.; Mao, F.; Wu, J.-K.; Xue, B. Fabrication of Na, Cl co-doped graphitic carbon nitride with enhanced photocatalytic activity for degradation of dyes and antibiotics. *J. Mater. Sci. Mater. Electron.* **2019**, *30*, 4446–4454. [CrossRef]
87. Zhang, S.; Li, J.; Zeng, M.; Li, J.; Xu, J.; Wang, X. Bandgap engineering and mechanism study of nonmetal and metal ion codoped carbon nitride: C+Fe as an example. *Chem. Eur. J.* **2014**, *20*, 9805–9812. [CrossRef]
88. Wu, W.; Ruan, Z.; Li, J.; Li, Y.; Jiang, Y.; Xu, X.; Li, D.; Yuan, Y.; Lin, K. In situ preparation and analysis of bimetal Co-doped mesoporous graphitic carbon nitride with enhanced photocatalytic activity. *Nano-micro Lett.* **2019**, *11*, 10. [CrossRef] [PubMed]
89. Li, P.; Wang, M.; Huang, S.; Su, Y. Phosphorus-and fluorine-co-doped carbon nitride: Modulated visible light absorption, charge carrier kinetics and boosted photocatalytic hydrogen evolution. *Dalton Trans.* **2021**, *50*, 14110–14114. [CrossRef] [PubMed]
90. Huang, J.; Li, D.; Li, R.; Zhang, Q.; Chen, T.; Liu, H.; Liu, Y.; Lv, W.; Liu, G. An efficient metal-free phosphorus and oxygen co-doped g-C_3N_4 photocatalyst with enhanced visible light photocatalytic activity for the degradation of fluoroquinolone antibiotics. *Chem. Eng. J.* **2019**, *374*, 242–253. [CrossRef]
91. Anitha, B.; Devi, L.G. Photocatalytic activity of fluorine doped SrTiO3 under the irradiation of UV/solar light: Extended visible light absorption by the bulk lattice F− ions and suppression of photogenerated charge carrier recombination by the surface F− ions. *Chem. Phys. Lett.* **2020**, *742*, 137138. [CrossRef]
92. Ding, K.; Wen, L.; Huang, M.; Zhang, Y.; Lu, Y.; Chen, Z. How does the B, F-monodoping and B/F-codoping affect the photocatalytic water-splitting performance of g-C_3N_4? *Phys. Chem. Chem. Phys.* **2016**, *18*, 19217–19226. [CrossRef]

93. Yang, Y.; Jin, H.; Zhang, C.; Gan, H.; Yi, F.; Wang, H. Nitrogen-deficient modified P–Cl co-doped graphitic carbon nitride with enhanced photocatalytic performance. *J. Alloys Compd.* **2020**, *821*, 153439. [CrossRef]
94. Tang, J.-Y.; Kong, X.Y.; Ng, B.-J.; Chew, Y.-H.; Mohamed, A.R.; Chai, S.-P. Midgap-state-mediated two-step photoexcitation in nitrogen defect-modified g-C_3N_4 atomic layers for superior photocatalytic CO_2 reduction. *Catal. Sci. Technol.* **2019**, *9*, 2335–2343. [CrossRef]
95. Huang, Y.; Yan, Q.; Yan, H.; Tang, Y.; Chen, S.; Yu, Z.; Tian, C.; Jiang, B. Layer Stacked Iodine and Phosphorus Co-doped C_3N_4 for Enhanced Visible-Light Photocatalytic Hydrogen Evolution. *ChemCatChem* **2017**, *9*, 4083–4089. [CrossRef]
96. Shi, L.; Liang, L.; Wang, F.; Ma, J.; Sun, J. Polycondensation of guanidine hydrochloride into a graphitic carbon nitride semiconductor with a large surface area as a visible light photocatalyst. *Catal. Sci. Technol.* **2014**, *4*, 3235–3243. [CrossRef]
97. Chen, X.; Liu, L.; Yu, P.Y.; Mao, S.S. Increasing solar absorption for photocatalysis with black hydrogenated titanium dioxide nanocrystals. *Science* **2011**, *331*, 746–750. [CrossRef]
98. Hu, Y.; Pan, Y.; Wang, Z.; Lin, T.; Gao, Y.; Luo, B.; Hu, H.; Fan, F.; Liu, G.; Wang, L. Lattice distortion induced internal electric field in TiO_2 photoelectrode for efficient charge separation and transfer. *Nat. Commun.* **2020**, *11*, 2129. [CrossRef]
99. Huang, J.; Li, D.; Li, R.; Chen, P.; Zhang, Q.; Liu, H.; Lv, W.; Liu, G.; Feng, Y. One-step synthesis of phosphorus/oxygen co-doped g-C_3N_4/anatase TiO_2 Z-scheme photocatalyst for significantly enhanced visible-light photocatalysis degradation of enrofloxacin. *J. Hazard. Mater.* **2020**, *386*, 121634. [CrossRef]
100. Hu, C.; Hung, W.-Z.; Wang, M.-S.; Lu, P.-J. Phosphorus and sulfur codoped g-C_3N_4 as an efficient metal-free photocatalyst. *Carbon* **2018**, *127*, 374–383. [CrossRef]
101. Jiang, L.; Yuan, X.; Zeng, G.; Chen, X.; Wu, Z.; Liang, J.; Zhang, J.; Wang, H.; Wang, H. Phosphorus-and sulfur-codoped g-C_3N_4: Facile preparation, mechanism insight, and application as efficient photocatalyst for tetracycline and methyl orange degradation under visible light irradiation. *ACS Sustain. Chem. Eng.* **2017**, *5*, 5831–5841. [CrossRef]
102. Raizada, P.; Sudhaik, A.; Singh, P.; Shandilya, P.; Saini, A.K.; Gupta, V.K.; Lim, J.-H.; Jung, H.; Hosseini-Bandegharaei, A. Fabrication of Ag_3VO_4 decorated phosphorus and sulphur co-doped graphitic carbon nitride as a high-dispersed photocatalyst for phenol mineralization and E. coli disinfection. *Sep. Purif. Technol.* **2019**, *212*, 887–900. [CrossRef]
103. Raizada, P.; Thakur, P.; Sudhaik, A.; Singh, P.; Thakur, V.K.; Hosseini-Bandegharaei, A. Fabrication of dual Z-scheme photocatalyst via coupling of BiOBr/Ag/AgCl heterojunction with P and S co-doped g-C_3N_4 for efficient phenol degradation. *Arab. J. Chem.* **2020**, *13*, 4538–4552. [CrossRef]
104. Raizada, P.; Sudhaik, A.; Singh, P.; Shandilya, P.; Gupta, V.K.; Hosseini-Bandegharaei, A.; Agrawal, S. Ag_3PO_4 modified phosphorus and sulphur co-doped graphitic carbon nitride as a direct Z-scheme photocatalyst for 2,4-dimethyl phenol degradation. *J. Photochem. Photobiol. A Chem.* **2019**, *374*, 22–35. [CrossRef]
105. Zhang, B.; Li, C.; Zhang, Y.; Yuan, M.; Wang, J.; Zhu, J.; Ji, J.; Ma, Y. Improved photocatalyst: Elimination of triazine herbicides by novel phosphorus and boron co-doping graphite carbon nitride. *Sci. Total Environ.* **2021**, *757*, 143810. [CrossRef]
106. Zhang, H.; Han, X.; Yu, H.; Zou, Y.; Dong, X. Enhanced photocatalytic performance of boron and phosphorous co-doped graphitic carbon nitride nanosheets for removal of organic pollutants. *Sep. Purif. Technol.* **2019**, *226*, 128–137. [CrossRef]
107. Dong, F.; Li, Y.; Wang, Z.; Ho, W.-K. Enhanced visible light photocatalytic activity and oxidation ability of porous graphene-like g-C_3N_4 nanosheets via thermal exfoliation. *Appl. Surf. Sci.* **2015**, *358*, 393–403. [CrossRef]
108. Wang, J.; Liu, Z.; Li, S.; Li, C.; Liu, S.; Feng, J.; Tan, R. Foam-like boron-doped g-C_3N_4 as acid-base cooperative catalyst for efficient nucleophilic addition in water. *Green Chem. Eng.* **2021**, *2*, 239–249. [CrossRef]
109. Du, J.; Li, S.; Du, Z.; Meng, S.; Li, B. Boron/oxygen-codoped graphitic carbon nitride nanomesh for efficient photocatalytic hydrogen evolution. *Chem. Eng. J.* **2021**, *407*, 127114. [CrossRef]
110. Sun, D.; Li, L.; Yu, Y.; Huang, L.; Meng, F.; Su, Q.; Ma, S.; Xu, B. B and cyano groups co-doped g-C_3N_4 with multiple defects for photocatalytic nitrogen fixation in ultrapure water without hole scavengers. *J. Colloid Interface Sci.* **2021**, *600*, 639–648. [CrossRef]
111. Guo, Q.; Zhang, Y.; Qiu, J.; Dong, G. Engineering the electronic structure and optical properties of g-C_3N_4 by non-metal ion doping. *J. Mater. Chem. C* **2016**, *4*, 6839–6847. [CrossRef]
112. Han, X.; Yao, C.; Yuan, A.; Xi, F.; Dong, X.; Liu, J. Enhanced charge separation ability and visible light photocatalytic performance of graphitic carbon nitride by binary S, B co-doping. *Mater. Res. Bull.* **2018**, *107*, 477–483. [CrossRef]
113. Babu, P.; Mohanty, S.; Naik, B.; Parida, K. Synergistic effects of boron and sulfur Co-doping into graphitic carbon nitride framework for enhanced photocatalytic activity in visible light driven hydrogen generation. *ACS Appl. Energy Mater.* **2018**, *1*, 5936–5947. [CrossRef]
114. Huang, Y.; Li, D.; Fang, Z.; Chen, R.; Luo, B.; Shi, W. Controlling carbon self-doping site of g-C_3N_4 for highly enhanced visible-light-driven hydrogen evolution. *Appl. Catal. B Environ.* **2019**, *254*, 128–134. [CrossRef]
115. Wu, J.; Li, N.; Zhang, X.-H.; Fang, H.-B.; Zheng, Y.-Z.; Tao, X. Heteroatoms binary-doped hierarchical porous g-C_3N_4 nanobelts for remarkably enhanced visible-light-driven hydrogen evolution. *Appl. Catal. B Environ.* **2018**, *226*, 61–70. [CrossRef]
116. Samanta, S.; Yadav, R.; Kumar, A.; Sinha, A.K.; Srivastava, R. Surface modified C, O co-doped polymeric g-C_3N_4 as an efficient photocatalyst for visible light assisted CO_2 reduction and H_2O_2 production. *Appl. Catal. B Environ.* **2019**, *259*, 118054. [CrossRef]
117. Jing, L.; Wang, D.; He, M.; Xu, Y.; Xie, M.; Song, Y.; Xu, H.; Li, H. An efficient broad spectrum-driven carbon and oxygen co-doped g-C_3N_4 for the photodegradation of endocrine disrupting: Mechanism, degradation pathway, DFT calculation and toluene selective oxidation. *J. Hazard. Mater.* **2021**, *401*, 123309. [CrossRef]

118. Zheng, X.; Zhang, Q.; Chen, T.; Wu, Y.; Hao, J.; Tan, C.; Chen, P.; Wang, F.; Liu, H.; Lv, W. A novel synthetic carbon and oxygen doped stalactite-like g-C_3N_4 for broad-spectrum-driven indometacin degradation. *J. Hazard. Mater.* **2020**, *386*, 121961. [CrossRef]
119. Yang, C.; Teng, W.; Song, Y.; Cui, Y. CI codoped porous g-C_3N_4 for superior photocatalytic hydrogen evolution. *Chin. J. Catal.* **2018**, *39*, 1615–1624. [CrossRef]
120. Zhang, G.; Savateev, A.; Zhao, Y.; Li, L.; Antonietti, M. Advancing the n→ π^* electron transition of carbon nitride nanotubes for H_2 photosynthesis. *J. Mater. Chem. A* **2017**, *5*, 12723–12728. [CrossRef]
121. Kang, Y.; Wang, W.; Li, J.; Imhanria, S.; Hao, Y.; Lei, Z. Ultrathin B, N co-doped porous carbon nanosheets derived from intumescent flame retardant for rechargeable Zn-air battery. *J. Power Sources* **2021**, *493*, 229665. [CrossRef]
122. Piri, M.; Heravi, M.M.; Elhampour, A.; Nemati, F. Silver nanoparticles supported on P, Se-codoped g-C_3N_4 nanosheet as a novel heterogeneous catalyst for reduction of nitroaromatics to their corresponding amines. *J. Mol. Struct.* **2021**, *1242*, 130646. [CrossRef]
123. Liu, Z.; Zhang, X.; Jiang, Z.; Chen, H.-S.; Yang, P. Phosphorus and sulphur co-doping of g-C_3N_4 nanotubes with tunable architectures for superior photocatalytic H_2 evolution. *Int. J. Hydrogen Energy* **2019**, *44*, 20042–20055. [CrossRef]
124. Zhou, P.; Meng, X.; Li, L.; Sun, T. P, S Co-doped g-C_3N_4 isotype heterojunction composites for high-efficiency photocatalytic H_2 evolution. *J. Alloys Compd.* **2020**, *827*, 154259. [CrossRef]
125. Sahoo, D.P.; Das, K.K.; Patnaik, S.; Parida, K. Double charge carrier mechanism through 2D/2D interface-assisted ultrafast water reduction and antibiotic degradation over architectural S, P co-doped g-C_3N_4/ZnCr LDH photocatalyst. *Inorg. Chem. Front.* **2020**, *7*, 3695–3717. [CrossRef]
126. Xu, X.; Wang, S.; Yu, X.; Dawa, J.; Gui, D.; Tang, R. Biosynthesis of Ag deposited phosphorus and sulfur co-doped g-C_3N_4 with enhanced photocatalytic inactivation performance under visible light. *Appl. Surf. Sci.* **2020**, *501*, 144245. [CrossRef]
127. Ganganboina, A.B.; Nguyen, M.D.; Nguyen, T.H.L.; Kuncoro, E.P.; Doong, R.-A. Boron and phosphorus co-doped one-dimensional graphitic carbon nitride for enhanced visible-light-driven photodegradation of diclofenac. *Chem. Eng. Journal* **2021**, *425*, 131520. [CrossRef]
128. Yi, F.; Gan, H.; Jin, H.; Zhao, W.; Zhang, K.; Jin, H.; Zhang, H.; Qian, Y.; Ma, J. Sulfur-and chlorine-co-doped g-C_3N_4 nanosheets with enhanced active species generation for boosting visible-light photodegradation activity. *Sep. Purif. Technol.* **2020**, *233*, 115997. [CrossRef]
129. Li, X.; Zhang, J.; Huo, Y.; Dai, K.; Li, S.; Chen, S. Two-dimensional sulfur-and chlorine-codoped g-C_3N_4/CdSe-amine heterostructures nanocomposite with effective interfacial charge transfer and mechanism insight. *Appl. Catal. B Environ.* **2021**, *280*, 119452. [CrossRef]
130. Wang, H.; Yang, C.; Li, M.; Chen, F.; Cui, Y. Enhanced photocatalytic hydrogen production of restructured B/F codoped g-C_3N_4 via post-thermal treatment. *Mater. Lett.* **2018**, *212*, 319–322. [CrossRef]
131. Cui, Y.; Wang, H.; Yang, C.; Li, M.; Zhao, Y.; Chen, F. Post-activation of in situ BF codoped g-C_3N_4 for enhanced photocatalytic H_2 evolution. *Appl. Surf. Sci.* **2018**, *441*, 621–630. [CrossRef]
132. Liu, Q.; Shen, J.; Yu, X.; Yang, X.; Liu, W.; Yang, J.; Tang, H.; Xu, H.; Li, H.; Li, Y. Unveiling the origin of boosted photocatalytic hydrogen evolution in simultaneously (S, P, O)-Codoped and exfoliated ultrathin g-C_3N_4 nanosheets. *Appl. Catal. B Environ.* **2019**, *248*, 84–94. [CrossRef]
133. Chu, Y.-C.; Lin, T.-J.; Lin, Y.-R.; Chiu, W.-L.; Nguyen, B.-S.; Hu, C. Influence of P, S, O-Doping on g-C_3N_4 for hydrogel formation and photocatalysis: An experimental and theoretical study. *Carbon* **2020**, *169*, 338–348. [CrossRef]
134. Ma, H.; Zhao, S.; Li, S.; Liu, N. A facile approach to synthesizing S–Co–O tridoped g-C_3N_4 with enhanced oxygen-free photocatalytic performance via a hydrothermal post-treatment. *RSC Adv.* **2015**, *5*, 79585–79592. [CrossRef]
135. Wu, Z.; Tong, Z.; Xie, Y.; Sun, H.; Gong, X.; Qin, P.; Liang, Y.; Yuan, X.; Zou, D.; Jiang, L. Efficient degradation of tetracycline by persulfate activation with Fe, Co and O co-doped g-C_3N_4: Performance, mechanism and toxicity. *Chem. Eng. J.* **2022**, *434*, 134732. [CrossRef]
136. Li, G.; Wang, B.; Zhang, J.; Wang, R.; Liu, H. Er-doped g-C_3N_4 for photodegradation of tetracycline and tylosin: High photocatalytic activity and low leaching toxicity. *Chem. Eng. J.* **2020**, *391*, 123500. [CrossRef]
137. Jin, R.; Hu, S.; Gui, J.; Liu, D. A convenient method to prepare novel rare earth metal ce-doped carbon nitride with enhanced photocatalytic activity under visible light. *Bull. Korean Chem. Soc.* **2015**, *36*, 17–23. [CrossRef]
138. Kuila, S.K.; Sarkar, R.; Kumbhakar, P.; Kumbhakar, P.; Tiwary, C.S.; Kundu, T.K. Photocatalytic dye degradation under sunlight irradiation using cerium ion adsorbed two-dimensional graphitic carbon nitride. *J. Environ. Chem. Eng.* **2020**, *8*, 103942. [CrossRef]
139. Li, G.; Wang, R.; Wang, B.; Zhang, J. Sm-doped mesoporous g-C_3N_4 as efficient catalyst for degradation of tylosin: Influencing factors and toxicity assessment. *Appl. Surf. Sci.* **2020**, *517*, 146212. [CrossRef]
140. Sarkar, R.; Kumari, S.; Kundu, T.K. Density functional theory based studies on the adsorption of rare-earth ions from hydrated nitrate salt solutions on g-C_3N_4 monolayer surface. *J. Mol. Graph. Model.* **2020**, *97*, 107577. [CrossRef]
141. Wang, B.; Cao, Q.; Li, G.; Zhang, J. Preparation of non-polluting Tb-doped mesoporous carbon nitride photocatalyst and study on the efficacy and mechanism of degradation of antibiotics in water. *Environ. Sci. Pollut. Res.* **2022**, *29*, 36337–36350. [CrossRef]
142. Wang, M.; Guo, P.; Zhang, Y.; Lv, C.; Liu, T.; Chai, T.; Xie, Y.; Wang, Y.; Zhu, T. Synthesis of hollow lantern-like Eu (III)-doped g-C_3N_4 with enhanced visible light photocatalytic perfomance for organic degradation. *J. Hazard. Mater.* **2018**, *349*, 224–233. [CrossRef] [PubMed]
143. Tang, J.-Y.; Guo, R.-T.; Pan, W.-G.; Zhou, W.-G.; Huang, C.-Y. Visible light activated photocatalytic behaviour of Eu (III) modified g-C_3N_4 for CO_2 reduction and H_2 evolution. *Appl. Surf. Sci.* **2019**, *467*, 206–212. [CrossRef]

144. Tang, J.; Zhou, W.; Guo, R.; Huang, C.; Pan, W.; Liu, P. An exploration on in-situ synthesis of europium doped g-C_3N_4 for photocatalytic water splitting. *Energy Procedia* **2019**, *158*, 1553–1558. [CrossRef]
145. Guo, P.; Zhao, F.; Hu, X. Boron-and europium-co-doped g-C_3N_4 nanosheets: Enhanced photocatalytic activity and reaction mechanism for tetracycline degradation. *Ceram. Int.* **2021**, *47*, 16256–16268. [CrossRef]
146. Cui, W.; Li, J.; Cen, W.; Sun, Y.; Lee, S.; Dong, F. Steering the interlayer energy barrier and charge flow via bioriented transportation channels in g-C_3N_4: Enhanced photocatalysis and reaction mechanism. *J. Catal.* **2017**, *352*, 351–360. [CrossRef]
147. Wu, K.; Chen, D.; Lu, S.; Fang, J.; Zhu, X.; Yang, F.; Pan, T.; Fang, Z. Supramolecular self-assembly synthesis of noble-metal-free (C, Ce) co-doped g-C_3N_4 with porous structure for highly efficient photocatalytic degradation of organic pollutants. *J. Hazard. Mater.* **2020**, *382*, 121027. [CrossRef]
148. Zhu, Z.; Ma, C.; Yu, K.; Lu, Z.; Liu, Z.; Huo, P.; Tang, X.; Yan, Y. Synthesis Ce-doped biomass carbon-based g-C_3N_4 via plant growing guide and temperature-programmed technique for degrading 2-Mercaptobenzothiazole. *Appl. Catal. B Environ.* **2020**, *268*, 118432. [CrossRef]
149. Pan, T.; Chen, D.; Fang, J.; Wu, K.; Feng, W.; Zhu, X.; Fang, Z. Facile synthesis of iron and cerium co-doped g-C_3N_4 with synergistic effect to enhance visible-light photocatalytic performance. *Mater. Res. Bull.* **2020**, *125*, 110812. [CrossRef]
150. Guo, P.; Zhao, F.; Hu, X. Fabrication of a direct Z-scheme heterojunction between MoS2 and B/Eu-g-C_3N_4 for an enhanced photocatalytic performance toward tetracycline degradation. *J. Alloys Compd.* **2021**, *867*, 159044. [CrossRef]
151. Lai, C.; Yan, H.; Wang, D.; Liu, S.; Zhou, X.; Li, X.; Zhang, M.; Li, L.; Fu, Y.; Xu, F. Facile synthesis of Mn, Ce co-doped g-C_3N_4 composite for peroxymonosulfate activation towards organic contaminant degradation. *Chemosphere* **2022**, *293*, 133472. [CrossRef]
152. Mafa, P.J.; Malefane, M.E.; Idris, A.O.; Liu, D.; Gui, J.; Mamba, B.B.; Kuvarega, A.T. Multi-elemental doped g-C_3N_4 with enhanced visible light photocatalytic Activity: Insight into naproxen Degradation, Kinetics, effect of Electrolytes, and mechanism. *Sep. Purif. Technol.* **2022**, *282*, 120089. [CrossRef]